A machine learning approach to the prediction of transport and thermodynamic processes in multiphysics systems- Heat transfer in a hybrid nanofluid flow in porous media

Rasool Alizadeh[1], Javad Mohebbi Najm Abad[2,*], Abolhasan Ameri[3], Mohammad Reza Mohebbi[4], Amirfarhang Mehdizadeh[5], Dan Zhao[6], Nader Karimi[7,8]

[1]Department of Mechanical Engineering, Quchan Branch, Islamic Azad University, Quchan, Iran

[2]Department of Computer Engineering, Quchan Branch, Islamic Azad University, Quchan, Iran

[3]Department of Chemical Engineering, Shiraz Branch, Islamic Azad University, Shiraz, Iran

[4]Department of Computer Science, University of Passau, Innstraße 41,94032 Passau, Germany

[5]School of Computing and Engineering, Civil and Mechanical Engineering Department, University of Missouri-Kansas City, Kansas City, MO 64110, United States

[6]College of Engineering, University of Canterbury, Christchurch, New Zealand

[7]School of Engineering and Materials Science, Queen Mary University of London, London E1 4NS, United Kingdom

[8]James Watt School of Engineering, University of Glasgow, Glasgow G12 8QQ, United Kingdom

Corresponding author: javad.mohebi@gmail.com

Phone number and e-mail address:

Mob: +989155130074

E-mail: javad.mohebi@gmail.com

Abstract

Comprehensive analyses of transport phenomena and thermodynamics of complex multiphysics systems are laborious and computationally intensive. Yet, such analyses are often required during the design of thermal and process equipment. As a remedy, this paper puts forward a novel approach to the prediction of transport behaviours of multiphysics systems, offering significant reductions in the computational time and cost. This is based on machine learning techniques that utilise the data generated by computational fluid dynamics for training purposes. The physical system under investigation includes a stagnation-point flow of a hybrid nanofluid ($Cu-Al_2O_3$/Water) over a blunt object embedded in porous media. The problem further involves mixed convection, entropy generation, local thermal non-equilibrium and non-linear thermal radiation within the porous medium. The SVR (Support Machine Vector) model is employed to approximate velocity, temperature, Nusselt number and shear-stress as well as entropy generation and Bejan number functions. Further, PSO meta-heuristic algorithm is applied to propose correlations for Nusselt number and shear stress. The effects of Nusselt number, temperature fields and shear stress on the surface of the blunt-body as well as thermal and frictional entropy generation are analysed over a wide range of parameters. Further, it is shown that the generated correlations allow a quantitative evaluation of the contribution of a large number of variables to Nusselt number and shear stress. This makes the combined computational and artificial intelligence (AI) approach most suitable for design purposes.

Keywords: Support Vector Regression; Particle Swarm Optimization; Artificial Intelligence; Hybrid Nanofluid; Porous Media.

Nomenclature

a	cylinder radius (m)	r	radial coordinate (m)

AI	Artificial Intelligence	Re	Freestream Reynolds number $Re = \frac{\bar{k}.a^2}{2\upsilon}$
ANN	Artificial Neural Network	R_d	radiation parameter $R_d = \frac{16\sigma^* T_\infty^3}{3k^*.k_s}$
A_1, A_2, A_3, A_4, A_5	Constants	$\dot{S}'''_0$	characteristic entropy generation rate $(W.K^{-1}.m^{-3})$
a_{sf}	interfacial area per unit volume of porous media (m^{-1})	$\dot{S}'''_{gen}$	rate of entropy generation $(W.K^{-1}.m^{-3})$
Be	Bejan number	SVR	Support Vector Regression
Bi	Biot number $Bi = \frac{h_{sf}a_{sf}.a}{4k_s}$	T	Temperature (K)
Br	Brinkman number$Br = \frac{\mu_f(\bar{k}.a)^2}{k_f(T_w - T_\infty)}$	u, w	velocity components along $(r - z)$-axis $(m.s^{-1})$
C_p	specific heat at constant pressure $(J.K^{-1}.kg^{-1})$	z	axial coordinate
Da	Darcy number	**Greek symbols**	
$f(\eta)$	function related to u-component of velocity	α	thermal diffusivity
$f'(\eta)$	function related to w-component of velocity	β	Thermal expansion coefficient
g	Gravitational acceleration $(m.s^{-2})$	γ	modified conductivity ratio $\gamma = \frac{k_f}{k_s}$
Gr	Grashof number $Gr = \frac{g.\beta_f.a^3.T_\infty}{16.\upsilon_f^2}$	η	similarity variable, $\eta = \left(\frac{r}{a}\right)^2$
h	heat transfer coefficient $(W.K^{-1}.m^{-2})$	$\theta(\eta)$	non-dimensional temperature

h_{sf}	interstitial heat transfer coefficient $(W.K^{-1}.m^{-2})$	θ_w	temperature parameter $\theta_w = \frac{T_w}{T_\infty}$
k	thermal conductivity $(W.K^{-1}.m^{-2})$	λ	Permeability parameter, $\lambda = \frac{a^2}{4k_1}$
$\bar{k}$	freestream strain rate (s^{-1})	λ_1	Dimensionless mixed convection parameter $\lambda_1 = \frac{Gr}{Re^2} = \frac{g.\beta_f.T_\infty}{16.\upsilon_f^2}$
k_1	permeability of the porous medium (m^2)	ε	porosity
k^*	the mean absorption coefficient,	μ	dynamic viscosity $(N.s.m^{-2})$
m	Shape factor	υ	kinematic viscosity $(m^2.s^{-1})$
MAE	Mean Absolute Error	ρ	fluid density $(Kg.m^{-3})$
$MRMR$	Minimum redundancy maximum relevance	σ	Shear stress Pa
N_G	entropy generation number$N_G = \frac{\dot{S}'''_{gen}}{\dot{S}'''_0}$	σ^*	Stefan–Boltzman constant
Nu	Nusselt number	ϕ_1, ϕ_2	Solid volume fraction of nanoparticles of nanoparticles 1 and 2.
p	fluid pressure Pa	φ	angular coordinate
P	non-dimensional fluid pressure	**Subscripts**	
P_0	The initial fluid pressure Pa	∞	far field
Pr	Prandtl number	f	base fluid
PSO	Particle Swarm Optimization	nf	nanofluid
q_w	heat flow at the wall $(W.m^{-2})$	hnf	nano-solid-particles

q_r	Thermal radiation ($W.m^{-2}$)	s	Solid
		w	condition on the surface of the cylinder

1. **Introduction**

Conventional analysis of heat transfer (HT) involves development of numerical or theoretical models of the systems followed by examination of the effects of pertinent parameters on the rate of HT. Although this approach has been applied to many problems successfully, it performs best for limited number of parameters. Of course, the existing computational tools do allow consideration of complex problems with multi-physics. However, interpretation of the computational results and the incurred computational cost introduce significant drawbacks. As a result there has been a tendency to avoid analyzing the problems in which several physical mechanisms can simultaneously affect transport processes. In engineering practice, however, such situations are frequently encountered. Here, a novel predictive tool based on computational fluid dynamics and artificial intelligence is presented. The tool is capable of predicting the complex behaviors of transport and thermodynamic systems with only a small fraction of the corresponding computational cost.

The system under investigation simultaneously utilises a few methods of HT enhancement including stagnation flow, porous media and nano-fluid. In the following, the literature on the combinations of these methods are briefly reviewed. Much attention has been paid to HT in porous media of industrial applications such as heat exchangers, reactors, burners, dryers and furnaces [1-3]. Further, applying nanofluids in the HT equipment is an effective method of HT enhancement [4-6]. Nanoparticles could improve the thermal conductivity of the base fluid [7, 8] and the contact surface area between solid and liquid is increased due to the existence of porous media [9]. These two factors significantly influence the efficiency of HT processes [10, 11]. Further, if the fluid flows around the quiescent zone, it can be called the stagnation-point flow (SPF) [12]. SPF of nanofluids is observed in various circumstances like stretching or shrinking surfaces, sheets, cylinders and rotating disks [13-16]. Sajjadi et al. utilised multi-walled carbon nanotubes–iron oxide/water nanofluid to numerically investigate the effect of nanoparticles on the rate of natural convection HT in porous media. Lattice Boltzmann procedure was applied as a solution strategy to study the effects of porosity, nanoparticle volume fraction, Hartmann number, Rayleigh number and Darcy number. The HT rate and the Nusselt number improved by enhancing the Darcy number, porosity, Rayleigh number and adding nanoparticles. However, the Hartmann number demonstrated an inverse trend and caused a decrease in Nusselt number [17]. In another study, Hayat et al. [18] simulated the impinging flow in the porous medium around a stretching plate to investigate both HT and flow characteristics using homotopy analysis method.

A report of simultaneous effects of suction and blowing SPF on the radiative HT of a shrinking sheet was published by Bhattacharyya and Layek [19]. The wall temperature showed increment by suction intensification. Manh et al. [20] numerically carried out a study about convection and radiation HT of a hybrid nanomaterial in a porous tank. These authors considered the effect of the Lorentz force in their simulation and showed that the HT augmented in the presence of radiation and increasing the Hartmann number decreased the Nusselt number. In another study, they modeled a hybrid Fe_3O_4/MWCNT (multi-walled carbon nanotubes) nanofluid flow through a porous medium including radiation and magnetic field [21].

Natural convection HT of the Al_2O_3-Cu-water as a hybrid nanofluid in a porous cavity was analysed by Mehryan et al. [22] interestingly, they showed that increasing the volume fractions of nanoparticles led to a reduction in HT. This suppression was attributed to the kind of porous medium employed in this study. Ashraf et al. [23] performed an analysis of a convection HT of a 3D Maxwell fluid radiative flow over a stretching sheet. They demonstrated the effects of various parameters on the physical quantities in their results. Zhang et al. analytically examined the effects of three different nanoparticles Cu, Ag and Al_2O_3 in water flow over a flat plate affected by magnetic field and radiative HT [24].

A hybrid nanofluid flow in a double-porous layers of a T-shaped porous medium was numerically analysed by Mehryan et al. [25] and its natural convection HT under the influence of a magnetic field was investigated using finite element method and non-equilibrium model. Higher intensities of the magnetic field and values of thermal conductivity ratio and lowering the solid-liquid interface convection parameter resulted in augmentation of HT. Makinde and Mishra [26] examined the radiation of a SPF with nanoparticles through a stretching surface. The base fluid (water) viscosity was considered to be variable. The effects of different parameters were studied to obtain their influences on the Nusselt and Sherwood numbers, skin friction, temperature, velocity and concentration of nanofluid. A cylindrical surface subjected to catalytic reaction was the case study of Alizadeh et al. [27] to investigate the convective HT of impinging flow. Their results illustrated the variations of velocity and concentration profiles and Sherwood and Nusselt numbers. They demonstrated the specific influence of Dufour and Soret effects and thermal non-equilibrium on the boundary layers and the values of dimensionless Nusselt and Sherwood numbers.

Aminian et al. presented an investigation of forced convection effects of a hybrid nanofluid containing Al_2O_3–CuO–water over a cylindrical porous media. Hartmann and Darcy numbers were the two basic parameters that dramatically influenced the HT enhancement in the porous medium [28]. In another study, Abbas et al. [29] scrutinized the convective/radiative HT of a Casson flow near the stagnation point of a stretching/shrinking sheet. One of the main features of this research was inclusion of temperature dependent chemical reaction. Sheri and Shamshuddin [30] discussed the free convection and magnetohydrodynamics analysis of a micropolar flow with transient chemical reaction over the vertical porous plate. The important point of their study was consideration of magnetic field, radiative HT and dissipation effects. A stretching cylinder surrounded by a porous media with SA-Al_2O_3 and SA-Cu non-Newtonian Casson fluids flowing through it was analytically modelled by Tlili et al. to check the chemical reaction and thermal radiation effects. Their results revealed that increasing the thermal slip, Reynolds number, volume fraction of nanoparticles and magnetic field intensity would reduce the Nusselt number and HT rate [31]. Muhammad et al. [32] performed an analysis of a Bioconvection flow of magnetized Carreau nanofluid under the influence of slip over a wedge with motile microorganisms. In another study, Akbarzadeh et al. [33] scrutinized the Convection of heat and thermodynamic irreversibilities in two-phase, turbulent nanofluid flows in solar heaters by corrugated absorber plates. Alizadeh et al. [34] analysed the entropy generation (EG) and HT of a flow around a cylinder embedded in porous materials. The specific characteristics of their research were thermal non-equilibrium, magnetohydrodynamics and mixed radiation/radiation HT in the porous medium.

The literature survey shows that although there exist attempts to examine multiphysics problems, comprehensiveness analysis is still very hard to achieve. This is due to the existence of multidimensional parametric space that requires very large number of simulations for proper coverage. To address this issue, a novel method of artificial neural network (ANN) has received more attention in recent years. It has been applied as an effective remedy in many multi-functional engineering problems such as turbulence [35], porous media [36], multiphase flows [37] and for analysis, prediction and optimization.

Artificial neural network has been previously utilised in some thermal systems such as heat exchangers, heat pumps, refrigeration and air-conditioning systems [38]. For instance, Ahmad et al. [39] studied the temperature distribution in a porous fin model using ANN. The heat generation and thermal conductivity were considered to be temperature dependent. The optimized sizing and material of the fins on the heat exchanger wall were the main results of this research. Abdollahi et al. investigated the variations of HT coefficient and pressure drop (PD) relevant to a channel fluid flow with internal grooves and curved deflectors installed on its surface. The ANN technique was applied for configuration of the deflectors to optimize the PD and HT rate [40]. In another study, the effect of 6 porous baffles in a shell and tube heat exchanger on the HT and PD was numerically analyzed by Mohammadi et al. with the aim of ANN. They represented the optimum conditions of the baffle cuts, porosity and permeability [41]. Abdollahi and Shams [42] utilized ANN method and genetic algorithm to optimize the best shape and angle of vortex generator and the nanoparticles volume fraction of a flow in a rectangular channel. For prediction of capillary pressure and permeability data of a multi-phase flow in a porous media, Liu et al. trained ANN method. They proposed two network structures for prediction of petro-physical properties [43]. Uysal and Korkmaz developed an ANN model to estimate the EG and HT of a fluid flow through a mini-channel. The hybrid Ag/MgO nanoparticles in the base fluid of water was considered as a nanofluid [44]. It follows that different types of ANNs such as Support Vector Regression (SVR) can be considered as a reliable and reasonable approach for prediction of the results in problems that are encountered with various and a large number of non-linear interconnected parameters.

The predictive capabilities offered by ANN could be employed to save the computational burden incurred in the analysis of complex problems. As an example, in this work, the transport of heat and thermodynamic irreversibility in a nanofluid flow over a blunt body embedded in porous media are investigated. The study includes development and use of a machine learning tool trained by the computationally generated data.

2. Mathematical modelling

2.1. Problem statement

A schematic configuration of the flow and heat transfer problem in this study is illustrated in Fig. 1. This is involved in a nanofluid flow around an embedded cylinder in a porous medium under radial HT. A Newtonian, single phase, laminar and steady nanofluid flow is considered. Local thermal non-equilibrium condition is assumed for a cylinder with infinite length and a homogenous and isotropic porous medium. The non-axisymmetric characteristics of the flow past the cylinder is due to non-uniformity of transpiration. It is further assumed that the gravity applies along the axis of cylinder. Although, there is an external axisymmetric radial SPF around the cylinder. Non-linear effects could be considered small in the momentum transfer because of the moderate range of Reynolds number in pore-scale. Finally, the thermal dispersion effects and flow kinetic energy viscous dissipation are ignored due to constant specific heat, porosity, thermal conductivity and density.

The solutions can be obtained by solving the governing equations as shown below.

The continuity of mass [36]:

$$\frac{\partial(ru)}{\partial r} + r\frac{\partial w}{\partial z} = 0 \tag{1}$$

The momentum equation in radial direction [36]:

$$\frac{\rho_{hnf}}{\varepsilon^2}\left(u\frac{\partial u}{\partial r} + w\frac{\partial u}{\partial z}\right) = -\frac{\partial p}{\partial r} + \frac{\mu_{hnf}}{\varepsilon}\left(\frac{\partial^2 u}{\partial r^2} + \frac{1}{r}\frac{\partial u}{\partial r} - \frac{u}{r^2} + \frac{\partial^2 u}{\partial z^2}\right) - \frac{\mu_{hnf}}{k_1}u \tag{2}$$

The axial direction momentum transport including buoyancy force [36]:

$$\frac{\rho_{hnf}}{\varepsilon^2}\left(u\frac{\partial w}{\partial r} + w\frac{\partial w}{\partial z}\right) = -\frac{\partial p}{\partial z} + \frac{\mu_{hnf}}{\varepsilon}\left(\frac{\partial^2 w}{\partial r^2} + \frac{1}{r}\frac{\partial w}{\partial r} + \frac{\partial^2 w}{\partial z^2}\right) \pm (\rho\beta)_{hnf}\, g\left(T_{hnf} - T_\infty\right) - \frac{\mu_{hnf}}{k_1} \tag{3}$$

The thermal energy transport in the porous medium is given by equations (4) and (5).

The nanofluid phase energy equation [36]:

$$u\frac{\partial T_{hnf}}{\partial r} + w\frac{\partial T_{hnf}}{\partial z} = \frac{k_{hnf}}{\left(\rho C_p\right)_{hnf}}\left(\frac{\partial^2 T_{hnf}}{\partial r^2} + \frac{1}{r}\frac{\partial T_{hnf}}{\partial r} + \frac{\partial^2 T_{hnf}}{\partial z^2}\right) + \frac{h_{sf}\,.\,a_{sf}}{\left(\rho C_p\right)_{hnf}}\left(T_s - T_{hnf}\right) \tag{4}$$

The solid phase thermal energy transport:

$$k_s\left(\frac{\partial^2 T_s}{\partial r^2}+\frac{1}{r}\frac{\partial T_s}{\partial r}+\frac{\partial^2 T_s}{\partial z^2}\right)-h_{sf}\,.\,a_{sf}\left(T_s-T_{hnf}\right)-\frac{1}{r}\frac{\partial}{\partial r}(r.q_r)=0 \tag{5}$$

The radiative heat flux applying Rosseland approximation [34]:

$$q_r=-\frac{4\sigma^*}{3k^*}\frac{\partial T_s^4}{\partial r} \tag{6}$$

Re-writing Eq.(5) leads to:

$$k_s\left(\frac{\partial^2 T_s}{\partial r^2}+\frac{1}{r}\frac{\partial T_s}{\partial r}+\frac{\partial^2 T_s}{\partial z^2}\right)-h_{sf}\,.\,a_{sf}\left(T_s-T_{hnf}\right)+\frac{1}{r}\frac{\partial}{\partial r}\left(r.\frac{16\sigma^*}{3k^*}T_s^3\frac{\partial T_s}{\partial r}\right)=0 \tag{7}$$

In the previous studies, the term T_s^4 in Eq. (6) is developed and linearized about the ambient temperature T_∞ [34-36]. However, a nonlinear form of thermal radiation has been taken into account in this work. In the above equations,p, T, μ_{nf}, ρ_{hnf},$k_{hnf}$and $\left(\rho C_p\right)_{hnf}$are the pressure, temperature, kinematic viscosity, density, thermal conductivity and heat capacitance of the hybrid nanofluid, respectively. The parameters β,q_r, g,T_∞,k^* and σ^* also denote thermal expansion coefficient, radiative heat flux, gravitational acceleration, prescribed temperature at the wall, the mean absorption coefficient and Stefan–Boltzmann constant, respectively. These properties are computed inside the boundary layer and nearby the flow impingement point.

The following conditions are applied for the hydrodynamic boundary conditions.

$$r=a:\quad w=0\ ,\quad u=0 \tag{8}$$

$$r=\infty:\quad w=2\bar{k}z\,,\quad u=-\bar{k}\left(r-\frac{a^2}{r}\right) \tag{9}$$

The no-slip conditions are assumed for the external surface of the cylinder based on Eq. (8), where Eq. (9) represents that as r→∞, the viscous flow solution approaches the potential flow solution [34, 36, 37].Integrating the continuity equation of $-\frac{1}{r}\frac{\partial(ru)}{\partial r}=\frac{\partial w}{\partial z}$ Constant = $2\bar{k}z$ in r and z directions verifies this matter.The boundary conditions of this integration are w=0 at z=0 and u=0 at r=a.

Also, Eq. (10) demonstrates the boundary conditions of the energy balance equation in the porous region:

$$\begin{aligned} r = a: \quad & T_{hnf} = T_w = \text{Constant} \\ & T_s = T_w = \text{Constant} \\ r = \infty: \quad & T_{hnf} = T_\infty \\ & T_s = T_\infty, \end{aligned} \tag{10}$$

Where T_w and T_∞ are the cylinder surface and free-stream temperatures.

2.2 Hybrid nanofluid

The hybrid nanofluid implemented in this study was achieved by taking the mixture of Cu nanoparticles into 0.1vol. of Al_2O_3/water. The boundary layer equations for this hybrid nanofluid were analysed by a special form of thermo physical properties. In this model, ϕ_1 is considered as the solid volume fraction of Al_2O_3 nanoparticle added to the base fluid and ϕ_2 indicates the various solid volume fractions of Cu added to form the hybrid nanofluid namely Cu−Al_2O_3/Water. Table 1 represents these equations needed for the determination of the effective thermo-physical properties of the nanofluid and hybrid nanofluid [31]. Where $m = 3$ represents for the spherical nanoparticles. Furthermore, Table 2 depicts the thermo-physical properties of the nanoparticles and the base fluid at 25 °C. In addition, Table 3 shows different shapes of the nanoparticles along with shape factor and sphericity parameters.

2.3 Self-similar solutions

Similarity transformations of the governing Eqs. (1-7) were carried out based on Eq. (11) to obtain the dimensionless Eqs. (12) and (13).

$$u = -\frac{\bar{k}.a}{\sqrt{\eta}} f(\eta), \qquad w = 2\bar{k}f'(\eta)z, \qquad p = \rho_f \bar{k}^2 a^2 P \tag{11}$$

where $\eta = \left(\frac{r}{a}\right)^2$ indicates the dimensionless radial variable.

Substituting Eq. (11) into Eqs. (2), (3) and (4) gives:

$$\varepsilon[\eta f''' + f''] + Re.A_1.A_2[1 + ff' - (f')^2] + \varepsilon^2.\lambda[1 - f'] \pm \varepsilon^2.A_5.\lambda_1.(\theta_w - 1)\theta_{hnf} = 0 \tag{12}$$

$$P - P_0 = -\frac{1}{2\varepsilon^2}\left(\frac{f^2}{\eta}\right) - \frac{1}{\varepsilon.A_1.A_2}\left[\left(\frac{f'}{Re}\right) + \frac{\lambda}{Re}\int_1^\eta \frac{f}{\eta} d\eta\right] - 2\left[\frac{1}{\varepsilon^2} + \frac{1}{A_1.A_2}\frac{\lambda}{Re}\right]\left(\frac{z}{a}\right)^2 \tag{13}$$

In which $Re = \frac{\bar{k}.a^2}{2\upsilon_f}$ is the free stream Reynolds number, $\lambda = \frac{a^2}{4k_1}$ denotes the reciprocal of Darcy number, the Grashof number is indicated by $Gr = \frac{g.\beta_f.a^3.T_\infty}{16.\upsilon_f^2}$ and $\lambda_1 = \frac{Gr}{Re^2} = \frac{g.\beta_f.T_\infty}{16.\upsilon_f^2}$ shows the dimensionless mixed convection. The prime introduces the differentiation with respect to η.

The boundary conditions for two above equations vary to the following forms with respect to Eqs. (8), (9), and (10):

$$\eta = 1: \qquad f'(1) = 0, \qquad f(1) = 0 \tag{14}$$

$$\eta \to \infty: \qquad f'(\infty) = 0 \tag{15}$$

where Eq. (4) can be non-dimensional. It is edusing the transformation of:

$$\theta(\eta) = \frac{T(\eta) - T_\infty}{T_w - T_\infty} \tag{16}$$

Thus, there is:

$$T(\eta) = T_\infty[1 + (\theta_w - 1)\theta] \tag{17}$$

Eq. (18) is found as a result of substituting Eqs. (11) and (17) into Eq. (4) by the aim of neglecting the small dissipation terms.

$$\eta\theta''_{hnf} + \acute{\theta}_{hnf} + Re.Pr.\frac{A_3}{A_4}.\left(f.\theta'_{hnf}\right) + \frac{Bi.\gamma}{A_3}\left(\theta_s - \theta_{hnf}\right) = 0 \tag{18}$$

The parameter $\theta_w = \frac{T_w}{T_\infty}$demonstrates the temperature parameter, $Bi = \frac{h_{sf}a_{sf}.a^2}{4k_s}$denotes the Biot number and $R_d = \frac{16\sigma^* T_\infty^3}{3k^*.k_s}$ stands for the radiative parameter. Hence, the thermal boundary conditions applied to the nanofluid phase can be expressed by the followings.

$$\eta = 1: \qquad \theta_{hnf}(1) = 1 \tag{19a}$$

$$\eta \to \infty: \qquad \theta_{hnf}(\infty) = 0 \tag{19b}$$

Substituting Eqs. (11) and (17) into Eq. (7) provides:

$$\eta\theta''_s + \theta'_s - Bi\left(\theta_s - \theta_{hnf}\right) + R_d.\frac{\partial}{\partial\eta}\left[\eta.(1 + (\theta_w - 1)\theta_s)^3.\acute{\theta}_s\right] = 0 \tag{20}$$

Here, $\gamma = \frac{k_s}{k_f}$ denotes the conductivity ratio.

Thermal boundary conditions applied to the solid phase of the porous medium are introduced as:

$$\eta = 1: \qquad \theta_s(1) = 1 \tag{21a}$$

$$\eta \to \infty: \qquad \theta_s(\infty) = 0 \tag{21b}$$

The constants of A_1, A_2, A_3, A_4 and A_5 in Eqs. (12), (13), (18) and (20) can be calculated as:

$$A_1 = (1-\phi_1)^{2.5}(1-\phi_2)^{2.5} \quad , \quad A_2 = (1-\phi_2)\left[(1-\phi_1) + \phi_1\left(\frac{\rho_{s_1}}{\rho_f}\right)\right] + \phi_2\left(\frac{\rho_{s_2}}{\rho_f}\right) \tag{22}$$

$$A_3 = (1-\phi_2)\left[(1-\phi_1) + \phi_1\frac{\left(\rho.C_p\right)_{s_1}}{\left(\rho.C_p\right)_f}\right] + \phi_2\frac{\left(\rho.C_p\right)_{s_2}}{\left(\rho.C_p\right)_f}$$

$$A_4 = \frac{k_{s_1} + (m-1)k_f - (m-1)\phi_1\left(k_f - k_{s_1}\right)}{k_{s_1} + (m-1)k_f + \phi_1\left(k_f - k_{s_1}\right)}.\frac{k_{s_2} + (m-1)k_{bf} - (m-1)\phi_2\left(k_{bf} - k_{s_2}\right)}{k_{s_2} + (m-1)k_{bf} + \phi_2\left(k_{bf} - k_{s_2}\right)}$$

$$A_5 = (1-\phi_2)\left[(1-\phi_1) + \phi_1 \frac{(\rho.\beta)_{s_1}}{(\rho.\beta)_f}\right] + \phi_2 \frac{(\rho.\beta)_{s_2}}{(\rho.\beta)_f}$$

An implicit and iterative tri-diagonal finite-difference scheme was employed for numerical solving of Eqs. (12), (18) and (20) by applying the boundary conditions (14), (15), (19) and (21).

2.4 Shear stress and Nusselt number

The following equation is suggested for shear-stress calculation on the cylinder external surface impinged by the nanofluid flow:

$$\sigma = \mu_{hnf}\left[\frac{\partial w}{\partial r}\right]_{r=a} \tag{23}$$

Where μ_{hnf} is used as the hybrid nanofluid viscosity. The following equation is proposed for the shear stress over the surface of cylinder using a semi-similar solution according to Eq. (11).

$$\sigma = \mu_{hnf}\frac{2}{a}\left[2\bar{k}zf''(1)\right] \Rightarrow \frac{\sigma.a}{4\mu_f\bar{k}z} = \frac{1}{A_1}f''(1) \tag{24}$$

The following relations can be used to calculate the local HT coefficient and the rate of HT.

$$h = \frac{q_w}{T_w - T_\infty} = \frac{-k_{hnf}\left(\frac{\partial T_{hnf}}{\partial r}\right)_{r=a}}{T_w - T_\infty} = -\frac{2k_{hnf}}{a}\frac{\partial \theta_{hnf}(1)}{\partial \eta} \tag{25}$$

$$q_w = -\frac{2k_{hnf}}{a}\frac{\partial \theta_{hnf}(1)}{\partial \eta}(T_w - T_\infty) \tag{26}$$

The Nusselt number is also shown as below:

$$Nu_{hnf} = \frac{h.a}{2k_f} = -\frac{k_{hnf}}{k_f}\theta'_{hnf}(1) = -A_3.\theta'_{hnf}(1) \tag{27}$$

2.5- Entropy generation (EG)

In the porous region, the following equation is presented to evaluate the volumetric rate of the local EG [34].

$$\dot{S}'''_{gen} = \frac{k_{hnf}}{{T_{hnf}}^2}\left(\frac{\partial T_{hnf}}{\partial r}\right)^2 + \frac{k_s}{{T_s}^2}\left[\left(\frac{\partial T_s}{\partial r}\right)^2 + \frac{16\sigma^*}{3k^*}T_s^3\left(\frac{\partial T_s}{\partial r}\right)^2\right] + h_{sf}a_{sf}\left(T_s - T_{hnf}\right)\left[\frac{1}{T_{hnf}} - \frac{1}{T_s}\right]$$
$$+\frac{2\mu_{hnf}}{T_\infty}\left[\left(\frac{\partial u}{\partial r}\right)^2 + \left(\frac{u}{r}\right)^2 + \left(\frac{\partial w}{\partial z}\right)^2 + \frac{1}{2}\left(\frac{\partial w}{\partial r}\right)^2\right] + \frac{\mu_{nf}}{k_1 T_\infty}\left[u^2 + w^2\right] \tag{28}$$

In which $N_G = \frac{\dot{S}'''_{gen}}{\dot{S}'''_0}$ and $\dot{S}'''_0 = \frac{8k_f.(T_w - T_\infty)^2 \upsilon_f}{\bar{k}.a^4.T_\infty^2}$ define the characteristic EG rate. The dimensionless form of the local EG (N_G) is defined as below through applying the similarly variables provided by Eqs. (11) and (28):

$$N_G = \frac{Re.A_4.\theta_w^2}{\left[1 + (\theta_w - 1)\theta_{hnf}\right]^2}\left[\eta\theta'^2_{hnf}\right]$$
$$+\frac{Re.\theta_w^2}{\gamma.[1 + (\theta_w - 1)\theta_s]^2}\Big[\eta\theta'^2_s$$
$$+\frac{R_d}{(\theta_w - 1)^2}\eta[1 + (\theta_w - 1)\theta_s]^3.[(\theta_w - 1).\theta'_s]^2\Big] \tag{29}$$
$$+ Bi.Re\frac{\theta_w^2}{(\theta_w - 1)}\left(\theta_s - \theta_{hnf}\right).\left[\frac{1}{1 + (\theta_w - 1)\theta_{hnf}} - \frac{1}{1 + (\theta_w - 1)\theta_s}\right]$$
$$+\frac{Re.Br.\theta_w}{(\theta_w - 1)}\frac{1}{A_1}\left\{\left[\eta f''^2 + 4f'^2 + \left(\frac{f}{\eta}\right)^2 - 2\frac{ff'}{\eta}\right] + \lambda\left[\left(\frac{f}{\eta}\right)^2 + 4f'^2\right]\right\}$$

The Brinkman number is expressed as $Br = \frac{\mu_f(\bar{k}.a)^2}{k_f(T_w - T_\infty)}$ in the above relation. The ratio of EG by HT to the total EG is introduced as the dimensionless number of the Bejan number. It is defined as:

$$Be = \left[\frac{Re.A_4.\theta_w^2}{[1+(\theta_w-1)\theta_{nf}]^2}\left[\eta\theta'^2_{hnf}\right] + \frac{Re.\theta_w^2}{\gamma.[1+(\theta_w-1)\theta_s]^2}\left[\eta\theta'^2_s + \frac{R_d}{(\theta_w-1)^2}\eta[1+(\theta_w-1)\theta_s]^3.[(\theta_w - 1).\theta'_s]^2\right]\right] / \left[\frac{Re.Br.\theta_w}{(\theta_w-1)}\frac{1}{A_1}\left\{\left[\eta f''^2 + 4f'^2 + \left(\frac{f}{\eta}\right)^2 - 2\frac{ff'}{\eta}\right] + \lambda\left[\left(\frac{f}{\eta}\right)^2 + 4f'^2\right]\right\}\right] \quad (30)$$

2.6 Grid independency and validation

The grid independency was verified using various mesh densities of 51×18, 102×36, 204×72, 408×144 and 816×288 in the numerical solutions. Variations of three different parameters of the dimensionless velocity and temperature with the mesh density are shown in Fig. 2. As it is obvious, no considerable changes in the dimensionless velocity and temperature are observed for (η, φ) grid sizes of (204×72), (408×144) and (816×288). Therefore, the mesh size of (408×144) in $\eta - \varphi$ directions was selected and applied to the numerical model. In order to manage high gradients around the cylinder external surface, a non-uniform mesh was fulfilled in η-direction. Although, φ direction was meshed uniform. The computational region was extended over $\varphi_{max} = 360°$ and $\eta_{max} = 15$, wherein η_{max} corresponding to $\eta \to \infty$. In all studied cases, the entire hydrodynamic and thermal boundary layers were considered for the computational domain. The computational mesh applied in this work is illustrated in Fig. 2. The error value of 10^{-7} was taken into account for the numerical solution convergence. The numerical error of the performed numerical scheme can be estimated as $O(\Delta\eta)^2$. The dimensionless velocity and temperature were compared with the literature results for the validation of the model, in which the flow pasts the infinitely large permeable cylinders with no transpiration were studied. The results of this comparison are illustrated in Fig. 3. This shows that the model results are in an excellent agreement with the literature data, which indicates the validation of the numerical simulations.

3. Artificial Intelligence techniques

In this section, the AI models used in this papers are introduced. It also explains how to use them to provide proposed equations to estimate Nusselt number and the dimensionless shear stress.

3.1 SVR (Support Vector Regression)

In this paper, the SVR which presented based on the Support Machine Vector model, is used for function approximation. SVR is an appropriate model to estimate nonlinear regression problems. The SVR model adjusts the minimum thickness curve to the data in such a way that the least error is created for the test data. In this regard, the M data set shown in Eq. (31) includes x_i input vectors and y_i corresponding output.

$$M = \begin{Bmatrix} (x_i, y_i) |\ i = 1,2, \dots, n \\ , x_i \in R^N , y_i \in R \end{Bmatrix} \tag{31}$$

n shows the number of the records in data sets. The goal of the regression analysis is to determine the function $f(x)$ in such a way that its estimated output has the least error compared to the desired output. The regression function can be introduced by the following equation in which δ is an uniform error with the distribution of $N(0, \sigma^2)$.

$$y_i = f(x_i) + \delta \tag{32}$$

Firstly, the inputs are mapped in a non-linear manner to a high-dimensional f-space that is linearly dependent on the output. For this purpose, Eq. (33) is utilized in which w and b are the weight vector and the bias value, respectively. Also, the $\varphi(\mathrm{x})$ is the function that maps the inputs from the space R to the space $R^{N\times h}$.

$$f(x_i) = w\varphi(x_i) + b | w \in R^{N\times h}, b \in R \tag{33}$$

A penalty function with Eq. (34) is defined for data that is outside the band.

$$L_\varepsilon(y_i, f(x_i)) = \begin{cases} 0 & |y_i - f(x_i)| \le \varepsilon \\ |y_i - f(x_i)| - \varepsilon & otherwise \end{cases} \tag{34}$$

In SVR, the goal is to find the function f in such a way that it deviates from the desired values by ε and is still linear. On the other hand, the empirical risk of the function f is calculated by Eq. (35).

$$R_{emp}[f] = \sum_{1}^{n} L_\varepsilon(y_i, f(x_i)) \tag{35}$$

C is the constant coefficient of the risk function. For data whose the value $|y - f(x_i)|$ are greater than ε, ξ_i^+or ξ_i^-, which are violation values. They are calculated by Eqs. (36) and (37).

$$\xi_i^+ = y - f(x_i) - \varepsilon \tag{36}$$

$$\xi_i^- = \varepsilon - y - f(x_i) \tag{37}$$

The penalty function is calculated using the violation values with Eq. (38).

$$L_\varepsilon(y_i, f(x_i)) = \xi_i^+ + \xi_i^- \tag{38}$$

Finally, the objective function for estimating the f function is calculated by Eq. (39):

$$minimize \frac{1}{2}\|w\|^2 + C\sum_{i=1}^{n}(\xi_i^+ + \xi_i^-) \tag{39}$$

S.t. $\forall i$ (40)

$$-y_i + f(x_i) + \varepsilon + \xi_i^+ \ge 0$$

$$y_i - f(x_i) + \varepsilon + \xi_i^- \ge 0$$

$$\xi_i^+, \xi_i^- \ge 0$$

To create the dual equation of Eq. (39), the Lagrange coefficients are calculated for each of the constraints, and then a simplification is performed. If α_i^+ and α_i^- are the coefficients of the first and second constraints of Eq. (39), respectively, the following equation is presented as

$$\begin{aligned} minimize \frac{1}{2}\sum_{i=1}^{n}\sum_{j=1}^{n}(\alpha_i^+ - \alpha_i^-)(\alpha_j^+ - \alpha_j^-) < \varphi(x_i)\cdot\varphi(x_j) > -\sum_{i=1}^{n}(\alpha_i^+ - \alpha_i^-)y_i \\ + \varepsilon\sum_{i=1}^{n}(\alpha_i^+ + \alpha_i^-) \end{aligned} \tag{41}$$

$$\text{S.t.}\begin{Bmatrix} \sum_{i=1}^{n}(\alpha_i^+ - \alpha_i^-) = 0 \\ \alpha^+ . \alpha^- \in [0, C] \end{Bmatrix}$$

For nonlinear problems, the Inner product of the two functions $\varphi(x_i)$ and $\varphi(x_j)$ is replaced by the Gaussian kernel function provided in Eq. (42).

$$K(x_i, x_j) = \exp\left(-\frac{\| x_i - x_j \|^2}{2\sigma^2}\right) \tag{42}$$

Finally, the function f is calculated by Eq. (43).

$$f(x) = \sum_{i=1}^{n}(\alpha_i^+ - \alpha_i^-)K(x_i, x) + b \tag{43}$$

In Eq. (43), b is calculated by following equation. SV is a support vector as

$$\begin{aligned} b = \frac{1}{n}\Bigg\{ \sum_{0<\alpha_i^-<C}\left[y_i - \sum_{x_j \in SV}(\alpha_j^+ - \alpha_j^-)K(x_i, x_j) - \varepsilon\right] \\ + \sum_{0<\alpha_i^+<C}\left[y_i - \sum_{x_j \in SV}(\alpha_j^+ - \alpha_j^-)K(x_i, x_j) + \varepsilon\right]\Bigg\} \end{aligned} \tag{44}$$

3.2 PSO (Particle Swarm Optimization)

The PSO as an evolutionary and metaheuristic algorithm is among the most powerful tools of artificial intelligence to solve optimization. PSO is used to work out many applications in various branches of science and engineering in duration.

In PSO, a number of particles are used to search the solution space. In order to have an optimum solution, particles move in the search spaces. Each particle has its own velocity and position. Also, each one remember the position called the personal best, in which it had the best result so far. Particle motion changes according to the information they exchange with each other. Particles know the position of the best solution they have found so far as the global best, based on the information they send to each other [45].

The PSO algorithm including several iterations to find sub-optimum solution of a problem. In the iteration t, each particle has to move to a new position based on the following equation:

$$V(t) = C_0 \times V(t-1) + C_1 \times rand \times \big(Pbest - Present(t-1)\big) + C_2 \times rand \times \big(Gbest - Present(t-1)\big) \tag{45}$$

$$Present(t) = Present(t-1) + V(t)$$

$V(t)$ and $Present(t)$ are the velocity and position of the particle in the ith iteration, respectively. C_i are coefficients used to calculate the particle velocity. C_0 is usually equal to one, C_1 and C_2 is about two. $rand$ is a function that generate a random number between zero and one. $Pbest$ and $Gbest$ are personal best and global best, respectively.

3.3 Estimating the Nusselt number and dimensionless shear stress

In this study, precise correlations are presented for the estimation of the Nusselt and Sherwood number. For each one, the following steps have been performed as:

- A list of the input parameters is prepared.
- The input parameters are prioritized using the MRMR (Minimum redundancy maximum relevance) algorithm [46, 47]. In this algorithm, one input parameter is

chosen in each step. The parameter is selected according to maximizing the amount of mutual information with the output parameter and minimizing it with the parameters that have been selected before.

- The prioritized parameters are fed into SVR model to estimate output parameter, which is the Nusselt or Sherwood. Estimation accuracy of the Nusselt and Sherwood numbers due to increase in the number of inputs can be analysed based on Figs. 4 and 5. In each of the figures, the number of the input parameters is displayed on the horizontal axis and the Mean Absolute Error (MAE) value calculated from the SVR model for estimation is shown on the vertical axis.

The MAE is calculated by following equation:

$$MAE = \frac{\sum_{i=1}^{n} |T_i - O_i|}{n}, \tag{46}$$

where n indicates the number of points evaluated and O_i and T_i depict the estimated and desired values, respectively. The proposed correlations can be applied in other similar problems to this study [46, 47].

According to the results as shown in Figs. 4 and 5, it can be pointed out that increasing the number of the features from more than a number cannot significantly improve the estimation of the output parameters. For example, the six first prioritized parameters are enough to estimate Nusselt value.

- Afterward, the following general equation has been proposed as:

$$Y = a_0 + a_1 \prod_{i=1}^{K} {X_i}^{P_i} \tag{47}$$

a_0 and a_1 are the coefficients. Y is Nusselt or Sherwood output parameter. X_i is the i-th input parameter. P_i is the power of input parameter X_i. K is the number of input parameters. The values of coefficients and powers are calculated using the PSO algorithm.The results of this experiment are shown in Tables 4-6.

The proposed equations were trained using the outputs of the numerical simulations. The number of the input parameters leads to various equations for the estimation of Nusselt and Sherwood numbers according to the prioritization of the features. The parameters related to Nusselt number estimation and correlations are summarized in Tables 7 and 8. Further, the parameters of Sherwood number estimation and correlation is depicted in Tables 9 and 10, which are more accurate due to the addition of the more parameters to the proposed correlations. The values of mean absolute error (MAE) indicate the criterion of correlations accuracy against true values of numerical simulations.

4. Result and discussions

The computational model developed in Sect. 2 was used to generate simulation data for several test cases. These were fed to the AI tool as described in Sect. 3 and the predictions obtained from this tool are presented in this section.

4.1.Thermohydraulics

Fig. 6 shows the surface plots of the dimensionless fluid temperature varying with different parameters. As it is obvious in Fig. 6a, Reynolds number increases result in a significant reduction of the dimensionless temperature for a given concentration of nanoparticles. Considering the definition of the dimensionless temperature (Eq. 16), this indicates that as Reynolds number increases the temperature at the probing point (see Table 2) approaches that of the free stream. This may initially sound counterintuitive, as a higher flow velocity usually causes a larger rates of HT and therefore should result in increasing the flow temperature towards the wall temperature. However, it is worthy that the thickness of the thermal boundary layer is affected by increases in the Reynolds number. Therefore, for a fixed point (as in this case), higher fluid velocity pushes the probing point to the top of the thermal boundary layer in which the temperature is lower and thus the dimensionless temperature is smaller. Fig. 6a further shows that higher values of nanoparticles concentrations leads to higher dimensionless temperature. This is in agreement with the previous studies reported [34-36]. Higher concentrations of nanofluid enhances the fluid thermal conductivity and thus boosts the HT and results in augmentation of the nanofluid temperature close the wall.

Fig. 6b shows that the variation of the dimensionless fluid temperature with Prandtl and Biot number is monotonic. However, this is not the case in Fig. 6c, in which the variation of the dimensionless fluid temperature with the radiation and mixed convection parameters have been shown for two different intensities of the magnetic field. Clearly, different patterns can be recognised depending upon the combination of parameters. For example, although at low Reynolds numbers, the dimensionless fluid temperature is increased with increase in mixed convection parameter, higher values of Reynolds number show the reversed trend. Fig. 6c shows that the relation between the dimensionless temperature of fluid and Biot number is non-monotonic. This provides a clear evidence on the complexity of thermal systems where the influencing parameters grow in number. This, in turn, reflects the practical difficulties associated with the conventional analyses and the major advantage that the current machine learning approach can offer.

The variations of dimensionless temperature of the porous medium solid phase, θ_s is illustrated in Fig. 7. Fig. 7a reveals that the variations of θ_s with Re number is rather minimal, regardless of the value of dimensionless wall temperature. However, according to Fig. 7a, the wall temperature parameter and θ_s can either increase or decrease with the radiation parameter. Fig. 7b confirms a gradual increase in θ_s as the concentrations of nanoparticles increases. This is due to the improvement of HT rate by addition of more nanoparticles and is in keeping with the result reported previously [48, 49].Further, increases in Reynolds number appear to boost the value of θ_s. Once again, this can be related to the influence of the flow velocity and Reynolds number upon the rate of HT [34-36].

Dependency of Nusselt number on a few parameters is depicted by Fig. 8. For a fixed Reynolds number, as the concentration of nanoparticles increases, there appears to be a linear growth in the value of Nusselt number. Further, as expected, increases in Reynolds number results in higher values of Nusselt number. As already discussed, this leads to large dimensionless temperatures for the fluid and porous solid phase. In the current problem, several quantities can impact Nusselt number and the graphical approaches such as that in Fig. 8 may lack comprehensiveness. For this reason, the AI tool developed in this work was used to generate a series of correlations (see Tables 8 and 10). These describe the mathematical relations between an increasing number of variables and the Nusselt number.

The shear stress over the cylinder external surface is relevant to the fluid dynamics of the problem. Nonetheless, the presence of the mixed convection relates fluid dynamics to HT and hence, all parameters influencing HT can affect the shear stress. This highly complicates the problem and makes the conventional analysis method quite lengthy and cumbersome. Fig. 9 shows that changes in the concentration of nanoparticles can have a considerable effect on the shear stress. The effect of the concentration of nanoparticles upon the temperature of nanofluids was already demonstrated (see Fig. 6). Given the dependency of momentum transport upon fluid temperature (see Eq. 3), it is unsurprising that concentration of nanoparticles can influence the shear stress on the cylinder. According to Fig. 9, increasing the nanoparticles concentration of results in reinforcement of the dimensionless shear stress. Further, as expected, higher values of Re number (flow velocity) render larger shear stress (Fig. 9b). Tables 7 and 8 present the developed correlations amongst the dimensionless shear stress and a number of pertinent parameters. It is clear that by increasing the number of considered parameters accuracy of the correlation increases and the mean absolute error drops.

4.2.Entropy generation (EG)

Fig. 10 depicts variation of EG number, N_G, with a few parameters. Fig. 10a demonstrates that amplification of permeability parameter (reduction of the permeability of the porous medium) increases the EG. It is also obvious that the value of EG number increases at higher Re numbers. Both of these trends are related to the augmentation of frictional entropy. As these effects are already well-understood they are not further discussed here. Fig. 10b also shows that enhancement in the concentration of nanoparticles results in stronger generation of entropy. This could be primarily attributed to the increases in the viscosity of nanofluid at higher concentration of nanoparticles, which intensifies the frictional EG. This figure further shows that, although to a limited extent, the radiation parameter can have a non-monotonic effect upon the generation of entropy.

Total generation of entropy involves the thermal and frictional components. Often, the relative importance of thermal EG is examined through analysis of Bejan number. Fig. 11 shows the outcome of such analysis, in which the same settings as Fig. 10 have been used. Fig. 11a illustrates that for large values of Brinkman number, the behaviour of Bejan number is in qualitative agreement with that of EG number in Fig. 10. However, in the limit of small Brinkman numbers a different trend is observed, in which the value of Bejan number declines at a higher Re number. Small Brinkman numbers can be viewed as a large difference between the wall and free stream temperatures, which lead to a strong potential for HT. For such case, the thermal EG is significant and thus parameters affecting HT could influence Bejan number as well. Reynolds number increment results in the intensification of the rate of HT and the relaxation of the local temperature gradients. This reduces the thermal EG, and results in the decline of Bejan number (see Fig. 10a). According to Fig. 11b, there is a non-trivial relation between Bejan number and Biot number, in which Bejan number is decreased from a small to moderate value of Biot number. However, this trend is reversed at higher values of Bejan number. Further, the nanoparticles volumetric concentration enhancement results in a growth in Bejan number. This could be described by paying attentions to the relation between the concentrations of nanoparticles and the values of dimensionless temperatures (as shown in Figs. 6 and 7) and Nusselt number (Fig. 8).

5. Conclusions

An artificial intelligence-based predictive model was developed for fast and accurate estimations of transport and thermodynamic processes in configurations involving complex multiphysics. As an example, a hybrid nanofluid flow passing over a cylinder embedded in porous media was considered in this work. A computational model of the problem was first developed through employing a semi-similarity technique. This included mixed convection and non-linear thermal radiation along with local thermal non-equilibrium in the porous medium. The computational results were then used to train an artificial intelligence tool developed through using supervised learning methods. Predictions made by this tool were then rigorously compared and validated against the computational data. The validated predictive tool was subsequently used to estimate the behaviours of temperature fields, Nusselt and Bejan number and, shear stress over the cylinder. This resulted in a significant reduction in the computational time (over 90%). Since the problem involves a large number of variables, these behaviours were observed to be complicated and involved non-monotonic trends. However, by using the artificial intelligence predictive tool, accurate correlations were developed for the key quantities. The correlations were presented in the ascending degree of accuracy through a consideration of a progressively larger number of variables. It is argued that the developed predictive tool is an efficient and practical alternative to purely computational tools used for the design of process equipment.

References

[1] A. Kasaeian, R. Daneshazarian, O. Mahian, L. Kolsi, A.J. Chamkha, S. Wongwises and I. Pop, Nanofluid flow and heat transfer in porous media: a review of the latest developments, Int. J. Heat Mass Transfer, 107 (2017) 778-791.

[2] H.J. Xu, Z.B. Xing, F.Q. Wang and Z.M. Cheng, Review on heat conduction, heat convection, thermal radiation and phase change heat transfer of nanofluids in porous media: Fundamentals and applications, Chem. Eng. Sci., 195 (2019) 462-483.

[3] B.G. Lougou, Y. Shuai, R. Pan, G. Chaffa and H. Tan, Heat transfer and fluid flow analysis of porous medium solar thermochemical reactor with quartz glass cover, Int. J. Heat Mass Transfer, 127 (2018) 61-74.

[4] T.A. Alkanhal, M. Sheikholeslami, A. Arabkoohsar, R.-u. Haq, A. Shafee, Z. Li and I. Tlili, Simulation of convection heat transfer of magnetic nanoparticles including entropy generation using CVFEM, Int. J. Heat Mass Transfer, 136 (2019) 146-156.

[5] T.D. Manh, N.D. Nam, K. Jacob, A. Hajizadeh, H. Babazadeh, M. Mahjoub, I. Tlili and Z. Li, Simulation of heat transfer in 2D porous tank in appearance of magnetic nanofluid, Physica A, 550 (2020) 123937.

[6] M. Sheikholeslami, M.B. Gerdroodbary, R. Moradi, A. Shafee and Z. Li, Application of Neural Network for estimation of heat transfer treatment of Al2O3-H2O nanofluid through a channel, Comput. Methods Appl. Mech. Eng., 344 (2019) 1-12.

[7] R.N. Radkar, B.A. Bhanvase, D.P. Barai and S.H. Sonawane, Intensified convective heat transfer using ZnO nanofluids in heat exchanger with helical coiled geometry at constant wall temperature, Mater. Sci. Energy Technol., 2 (2019) 161-170.

[8] A. Komeilibirjandi, A.H. Raffiee, A. Maleki, M.A. Nazari and M.S. Shadloo, Thermal conductivity prediction of nanofluids containing CuO nanoparticles by using correlation and artificial neural network, J. Therm. Anal. Calorim., 139 (2020) 2679-2689.

[9] M. Mesgarpour, A. Heydari and S. Saddodin, Investigating the effect of connection type of a sintered porous fin through a channel on heat transfer and fluid flow, J. Therm. Anal. Calorim., 135 (2019) 461-474.

[10] A. Elliott, M. Torabi, N. Karimi and S. Cunningham, On the effects of internal heat sources upon forced convection in porous channels with asymmetric thick walls, Int. Commun. Heat Mass Transfer, 73 (2016) 100-110.

[11] N. Karimi, Y. Mahmoudi and K. Mazaheri, Temperature fields in a channel partially filled with a porous material under local thermal non-equilibrium condition–An exact solution, Proceedings of the Institution of Mechanical Engineers, Part C: Journal of Mechanical Engineering Science, 228 (2014) 2778-2789.

[12] N. Abbas, M.Y. Malik, M.S. Alqarni and S. Nadeem, Study of three dimensional stagnation point flow of hybrid nanofluid over an isotropic slip surface, Physica A, (2020) 124020.

[13] M. Valizadeh Ardalan, R. Alizadeh, A. Fattahi, N. Adelian Rasi, M.H. Doranehgard and N. Karimi, Analysis of unsteady mixed convection of Cu–water nanofluid in an oscillatory, lid-driven enclosure using lattice Boltzmann method, J. Therm. Anal. Calorim., (2020) 1-17.

[14] A. Hafeez, M. Khan and J. Ahmed, Stagnation point flow of radiative Oldroyd-B nanofluid over a rotating disk, Comput. Methods Programs Biomed., 191 (2020) 105342.

[15] R. Alizadeh, S.R. Gomari, A. Alizadeh, N. Karimi and L.K.B. Li, Combined heat and mass transfer and thermodynamic irreversibilities in the stagnation-point flow of Casson rheological fluid over a cylinder with catalytic reactions and inside a porous medium under local thermal nonequilibrium, Comput. Math. Appl., 81 (2019) 786-810.

[16] T. Hayat, M.I. Khan, M. Waqas, A. Alsaedi and M. Farooq, Numerical simulation for melting heat transfer and radiation effects in stagnation point flow of carbon–water nanofluid, Comput. Methods Appl. Mechanics Eng., 315 (2017) 1011-1024.

[17] H. Sajjadi, A.A. Delouei, M. Izadi and R. Mohebbi, Investigation of MHD natural convection in a porous media by double MRT lattice Boltzmann method utilizing MWCNT–Fe3O4/water hybrid nanofluid, Int. J. Heat Mass Transfer, 132 (2019) 1087-1104.

[18] T. Hayat, Z. Abbas, I. Pop and S. Asghar, Effects of radiation and magnetic field on the mixed convection stagnation-point flow over a vertical stretching sheet in a porous medium, Int. J. Heat Mass Transfer, 53 (2010) 466-474.

[19] K. Bhattacharyya and G.C. Layek, Effects of suction/blowing on steady boundary layer stagnation-point flow and heat transfer towards a shrinking sheet with thermal radiation, Int. J. Heat Mass Transfer, 54 (2011) 302-307.

[20] T.D. Manh, N.D. Nam, G.K. Abdulrahman, M.H. Khan, I. Tlili, A. Shafee, M. Shamlooei and T. Nguyen-Thoi, Investigation of hybrid nanofluid migration within a porous closed domain, Physica A, 551 (2020) 123960.

[21] T.D. Manh, I. Tlili, A. Shafee, T. Nguyen-Thoi and H. Hamouda, Modeling of hybrid nanofluid behavior within a permeable media involving buoyancy effect, Physica A, 554 (2020) 123940.

[22] S.A.M. Mehryan, F.M. Kashkooli, M. Ghalambaz and A.J. Chamkha, Free convection of hybrid Al2O3-Cu water nanofluid in a differentially heated porous cavity, Adv. Powder Technol., 28 (2017) 2295-2305.

[23] M.B. Ashraf, T. Hayat, S.A. Shehzad and A. Alsaedi, Mixed convection radiative flow of three dimensional Maxwell fluid over an inclined stretching sheet in presence of thermophoresis and convective condition, AIP Adv., 5 (2015) 027134.

[24] C. Zhang, L. Zheng, X. Zhang and G. Chen, MHD flow and radiation heat transfer of nanofluids in porous media with variable surface heat flux and chemical reaction, Appl. Math. Modell., 39 (2015) 165-181.

[25] S.A.M. Mehryan, M.A. Sheremet, M. Soltani and M. Izadi, Natural convection of magnetic hybrid nanofluid inside a double-porous medium using two-equation energy model, J. Mol. Liq., 277 (2019) 959-970.

[26] O.D. Makinde and S.R. Mishra, On stagnation point flow of variable viscosity nanofluids past a stretching surface with radiative heat, Int. J. Appl. Comput. Math., 3 (2017) 561-578.

[27] R. Alizadeh, N. Karimi, A. Mehdizadeh and A. Nourbakhsh, Analysis of transport from cylindrical surfaces subject to catalytic reactions and non-uniform impinging flows in porous media, J. Therm. Anal. Calorim., 138 (2019) 659-678.

[28] E. Aminian, H. Moghadasi and H. Saffari, Magnetic field effects on forced convection flow of a hybrid nanofluid in a cylinder filled with porous media: a numerical study, J. Therm. Anal. Calorim., (2020) 1-13.

[29] Z. Abbas, M. Sheikh and S.S. Motsa, Numerical solution of binary chemical reaction on stagnation point flow of Casson fluid over a stretching/shrinking sheet with thermal radiation, Energy, 95 (2016) 12-20.

[30] S. Sheri and M.D. Shamshuddin, Finite element analysis on transient magnetohydrodynamic (MHD) free convective chemically reacting micropolar fluid flow past a vertical porous plate with Hall current and viscous dissipation, Propul. Power Res., 7 (2018) 353-365.

[31] I. Tlili, W.A. Khan and I. Khan, Multiple slips effects on MHD SA-Al2O3 and SA-Cu non-Newtonian nanofluids flow over a stretching cylinder in porous medium with radiation and chemical reaction, Results Phys., 8 (2018) 213-222.

[32] T. Muhammad, SZ. Alamri, H. Waqas, D. Habib, and R. Ellahi, Bioconvection flow of magnetized Carreau nanofluid under the influence of slip over a wedge with motile microorganisms, J. Therm. Anal. Calorim. 143(2021) 945-957.

[33] M. Akbarzadeh, S. Rashidi, N. Karimi, and R. Ellahi, Convection of heat and thermodynamic irreversibilities in two-phase, turbulent nanofluid flows in solar heaters by corrugated absorber plates, Adv. Powder Technol. 29 (2018) 2243-2254.

[34] R. Alizadeh, N. Karimi and A. Nourbakhsh, Effects of radiation and magnetic field on mixed convection stagnation-point flow over a cylinder in a porous medium under local thermal non-equilibrium, Journal of Thermal Analysis and Calorimetry

(2019) 1-21.

[35] M. Milano and P. Koumoutsakos, Neural network modeling for near wall turbulent flow, J. Comput. Phys., 182 (2002) 1-26.

[36] R. Alizadeh, J. Mohebbi Najm Abad, A. Fattahi, E. Alhajri and N. Karimi, Application of Machine Learning to Investigation of Heat and Mass Transfer Over a Cylinder Surrounded by Porous Media—The Radial Basic Function Network, J. Energy Res. Technol., 142 (2020) 112109.

[37] J.M.N. Abad, R. Alizadeh, A. Fattahi, M.H. Doranehgard, E. Alhajri and N. Karimi, Analysis of transport processes in a reacting flow of hybrid nanofluid around a bluff-body embedded in porous media using artificial neural network and particle swarm optimization, J. Mol. Liq., 313 (2020) 113492.

[38] M. Mohanraj, S. Jayaraj and C. Muraleedharan, Applications of artificial neural networks for refrigeration, air-conditioning and heat pump systems—a review, Renewable Sustainable Energy Rev., 16 (2012) 1340-1358.

[39] I. Ahmad, H. Zahid, F. Ahmad, M.A.Z. Raja and D. Baleanu, Design of computational intelligent procedure for thermal analysis of porous fin model, Chin. J. Phys., 59 (2019) 641-655.

[40] A. Abdollahi, M. Shams and A. Abdollahi, Artificial neural network modeling of a deflector in a grooved channel as well as optimization of its effective parameters, Heat Mass Transfer, 54 (2018) 59-68.

[41] M.H. Mohammadi, H.R. Abbasi, A. Yavarinasab and H. Pourrahmani, Thermal optimization of shell and tube heat exchanger using porous baffles, Appl. Therm. Eng., 170 (2020) 115005.

[42] A. Abdollahi and M. Shams, Optimization of heat transfer enhancement of nanofluid in a channel with winglet vortex generator, Appl. Therm. Eng., 91 (2015) 1116-1126.

[43] S. Liu, A. Zolfaghari, S. Sattarin, A.K. Dahaghi and S. Negahban, Application of neural networks in multiphase flow through porous media: Predicting capillary pressure and relative permeability curves, J. Pet. Sci. Eng., 180 (2019) 445-455.

[44] C. Uysal and M.E. Korkmaz, Estimation of entropy generation for Ag-MgO/water hybrid nanofluid flow through rectangular minichannel by using artificial neural network, Politeknik Dergisi, 22 (2019) 41-51.

[45] T.V. Sibalija, Particle swarm optimisation in designing parameters of manufacturing processes: A review (2008–2018), Appl. Soft Comput., 84 (2019) 105743.

[46] M.H. Hassoun, Fundamentals of artificial neural networks, MIT press, Cambridge, Massachusetts, 1995.

[47] A.Y. Alanis, N. Arana-Daniel and C. Lopez-Franco, Artificial neural networks for engineering applications, Academic Press, Cambridge, Massachusetts, 2019.

[48] D.G.P. Guthrie, M. Torabi and N. Karimi, Combined heat and mass transfer analyses in catalytic microreactors partially filled with porous material-The influences of nanofluid and different porous-fluid interface models, Int. J. Therm. Sci., 140 (2019) 96-113.

[49] L. Govone, M. Torabi, L. Wang and N. Karimi, Effects of nanofluid and radiative heat transfer on the double-diffusive forced convection in microreactors, J. Therm. Anal. Calorim., 135 (2019) 45-59.

[50] S. Rashidi, M. Bovand, and J.A. Esfahani, Opposition of Magnetohydrodynamic and AL_2O_3–water nanofluid flow around a vertex facing triangular obstacle, J. Mol. Liq. 215 (2016) 276-284.

[51] R.P. Laein, S. Rashidi, and J.A. Esfahani, Experimental investigation of nanofluid free convection over the vertical and horizontal flat plates with uniform heat flux by PIV, Adv. Powder Technol. 27 (2016) 312-322.

[52] S.Z. Shirejini, S. Rashidi, and J.A. Esfahani, Recovery of drop in heat transfer rate for a rotating system by nanofluids, J. Mol. Liq. 220 (2016) 961-969.

[53] R.S.R. Gorla, Heat transfer in an axisymmetric stagnation flow on a cylinder, Appl. Sci. Res. 32 (1976) 541–553.

[54] M. Bovand, S. Rashidi, and J.A. Esfahani, Optimum interaction between magnetohydrodynamics and nanofluid for thermal and drag management, J. Thermophys. Heat Transfer. 31 (2017) 218-229.

[55] S. Rashidi, M. Bovand, and J.A. Esfahani, Structural optimization of nanofluid flow around an equilateral triangular obstacle, Energy, 88 (2015) 385-398.

[56] M. Maskaniyan, S. Rashidi, and J.A Esfahani, A two-way couple of Eulerian-Lagrangian model for particle transport with different sizes in an obstructed channel, Powder Technol. 312 (2017) 260-269.

[57] S. Rashidi, M. Bovand, J.A. Esfahani, and G. Ahmadi, Discrete particle model for convective AL2O3–water nanofluid around a triangular obstacle, Appl. Therm. Eng. 100 (2016) 39-54.

[58] M. Bovand, S. Rashidi, G. Ahmadi, and J.A. Esfahani, Effects of trap and reflect particle boundary conditions on particle transport and convective heat transfer for duct flow-A two-way coupling of Eulerian-Lagrangian model, Appl. Therm. Eng. 108 (2016) 368-377.

[59] MN .Amar, MA Ghriga, H. Ouaer. On the evaluation of solubility of hydrogen sulfide in ionic liquids using advanced committee machine intelligent systems, J. Taiwan Inst. Chem. Eng. 118 (2021) 159-168.

[60] H. Mehrjoo, M. Riazi, MN. Amar, and AH. Sarapardeh, Modeling interfacial tension of methane-brine systems at high pressure and high salinity conditions, J. Taiwan Inst. Chem. Eng. 114 (2020) 125-141.

[61] Ghadikolaei, S. S., Yassari, M., Sadeghi, H., Hosseinzadeh, K., & Ganji, D. D., 2017. Investigation on thermophysical properties of Tio2–Cu/H2O hybrid nanofluid transport dependent on shape factor in MHD stagnation point flow. Powder technology, 322, pp. 428-438.

[62] Bergman, T.L., Incropera, F.P., Lavine, A.S. and DeWitt, D.P., 2011. Introduction to heat transfer. John Wiley & Sons

Figures

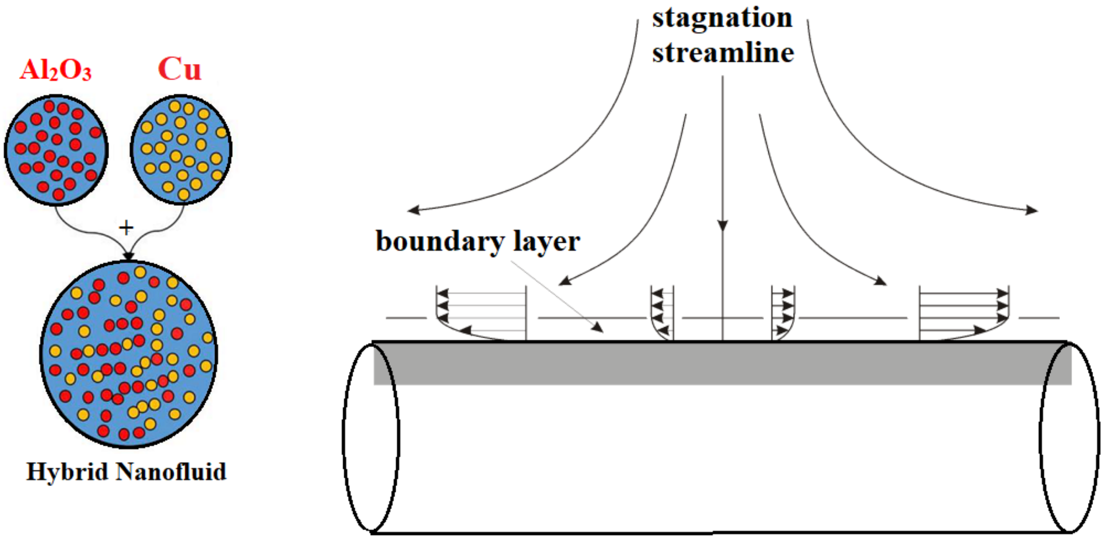

Fig. 1. The schematic representation of a blunt object (cylinder) under stagnation-point flow of hybrid nanofluid inside a porous medium.

1

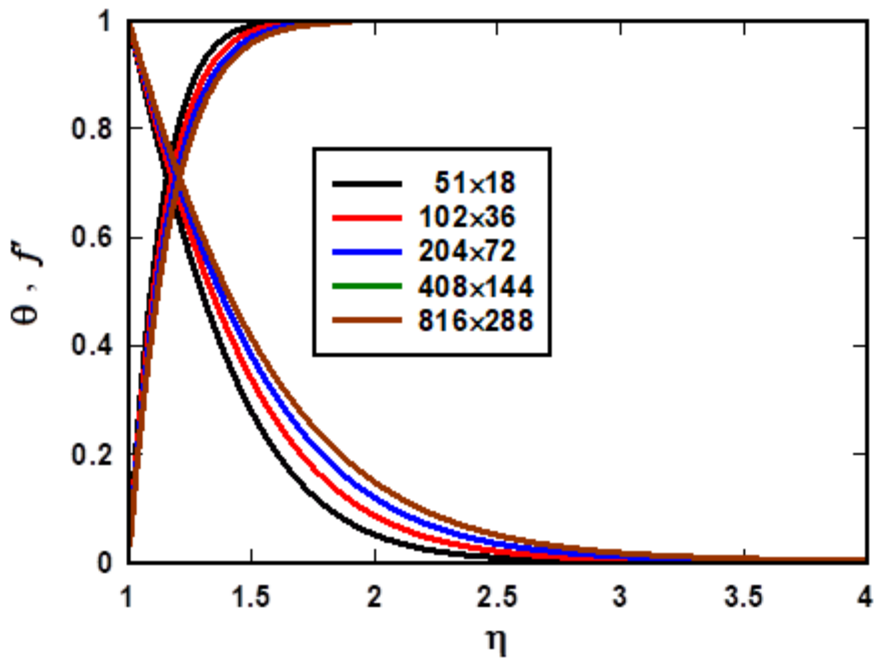

Fig. 2. Mesh independency analysis at $Re = 10$, $\lambda = 10$, $\lambda_1 = 1.0$, $M = 1.0$, $Bi = 0.1$, $R_d = 1.0$, $\theta_w = 1.2$

2

(a)

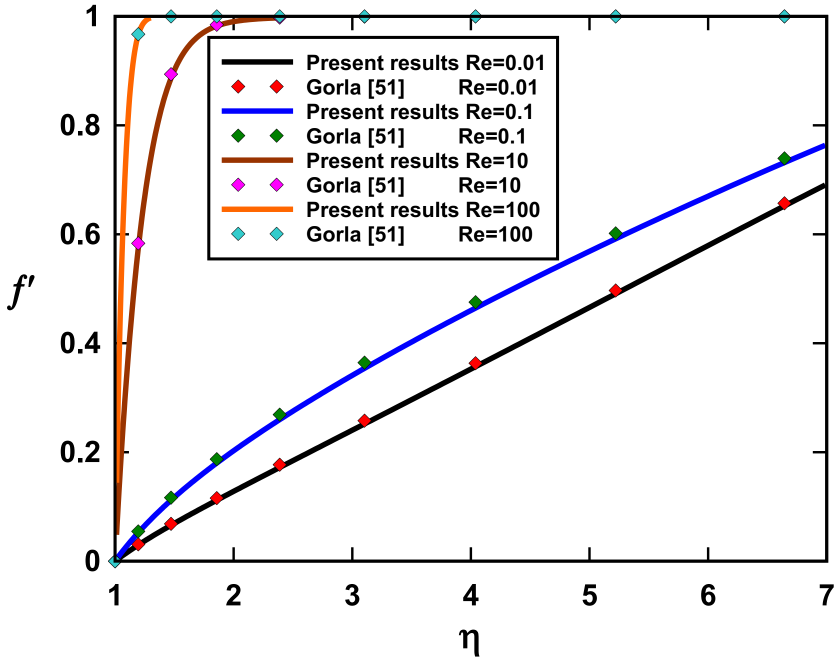

(b)

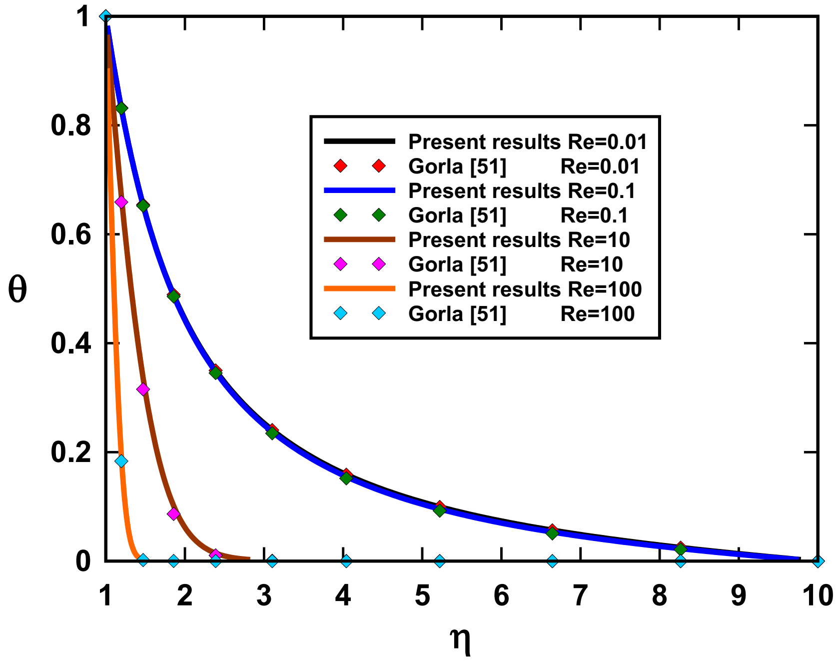

Fig. 3. A comparison between the current simulations and those of Ref. [51] for very large porosity and permeability.

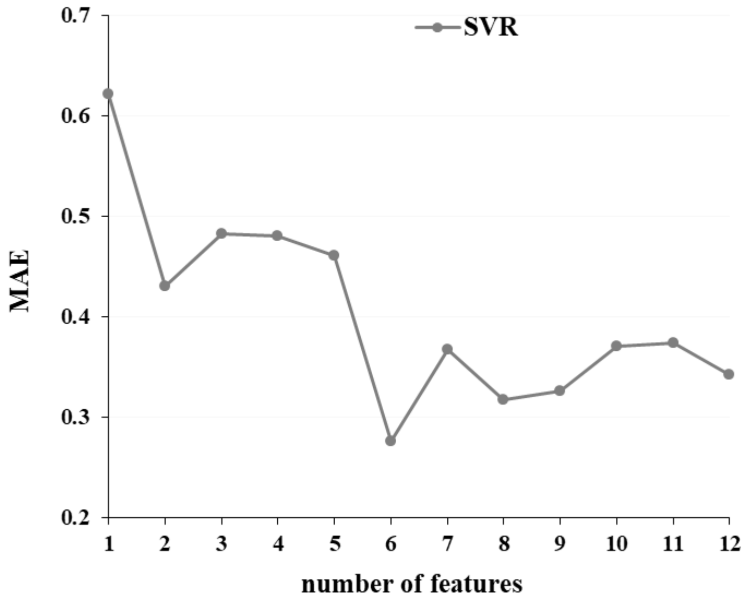

Fig. 4. Mean absolute error (MAE) for estimation of Nu for SVR model.

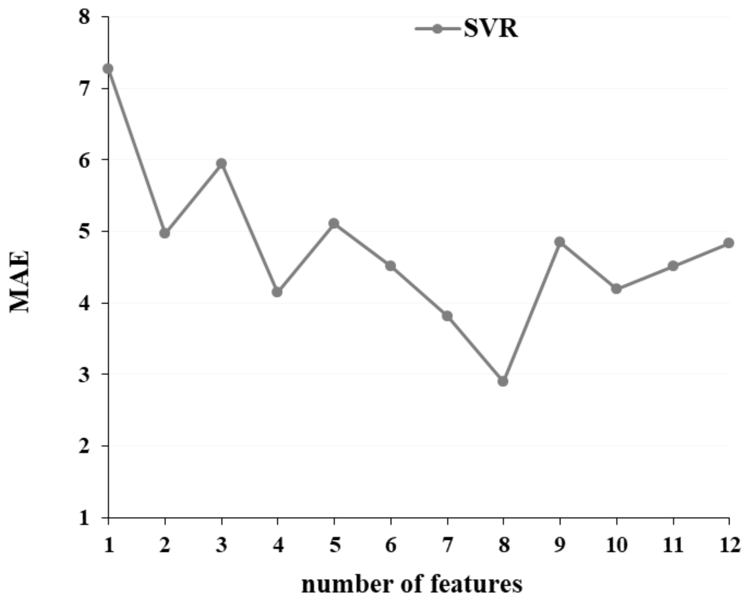

Fig. 5. Mean absolute error (MAE) for estimation of shear-stress for SVR model.

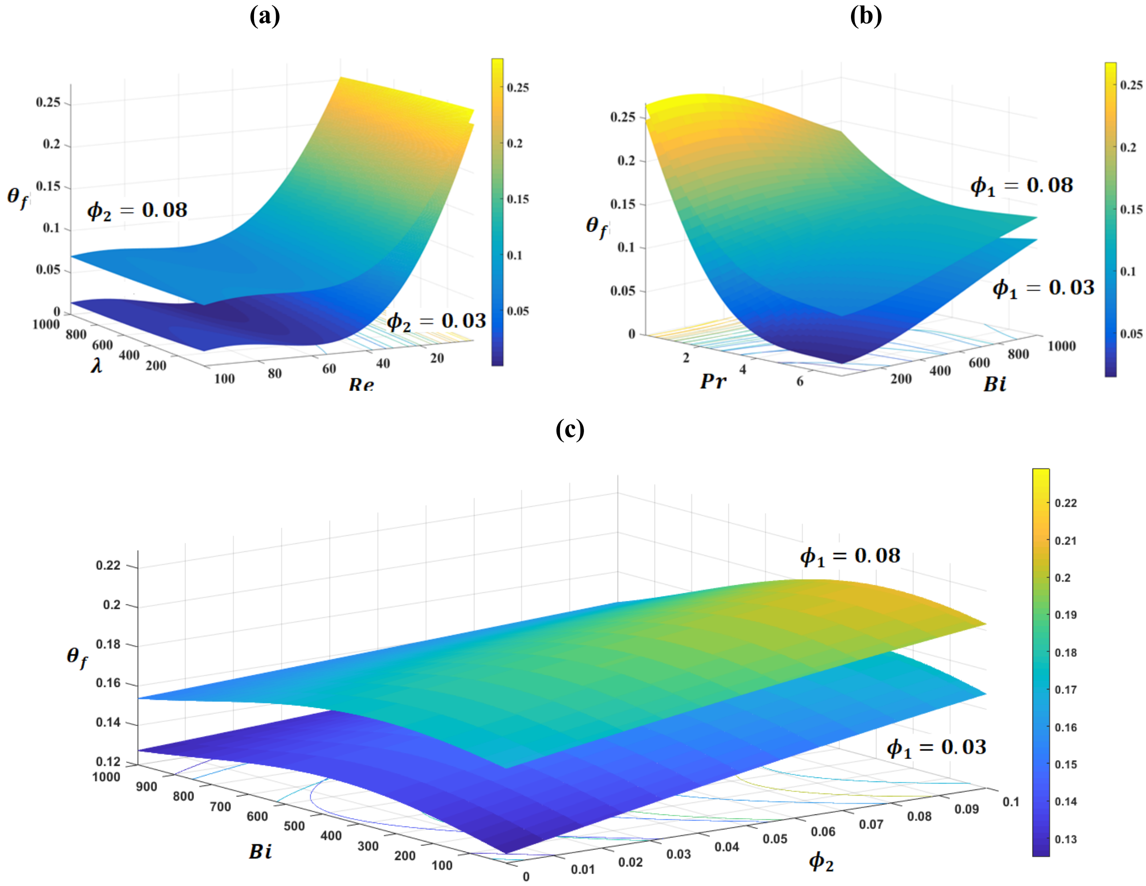

Fig. 6. Variation of the dimensionless fluid temperature with different pertinent variables.

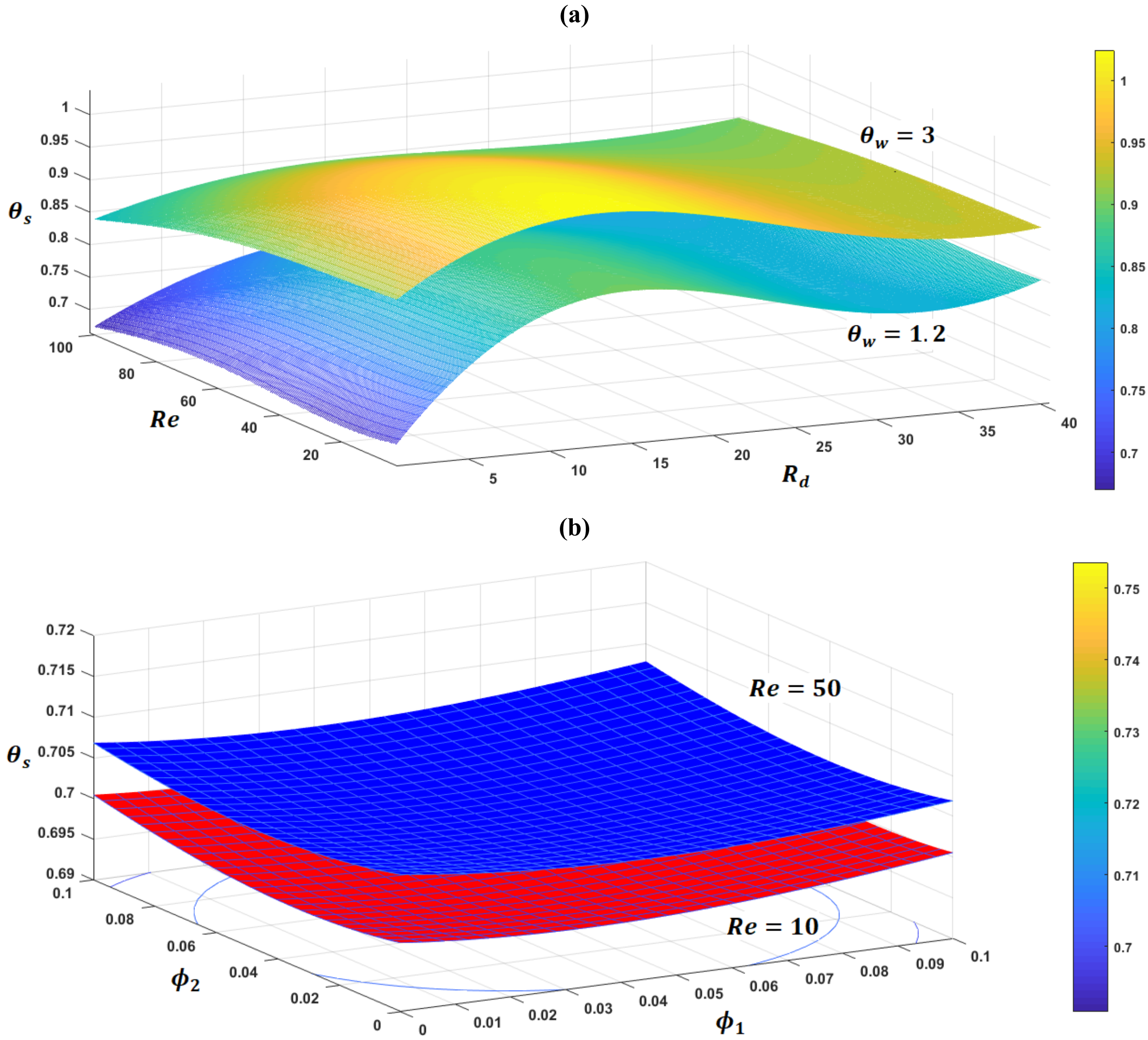

Fig. 7. Variation of dimensionless solid temperature with different pertinent variables.

(a)

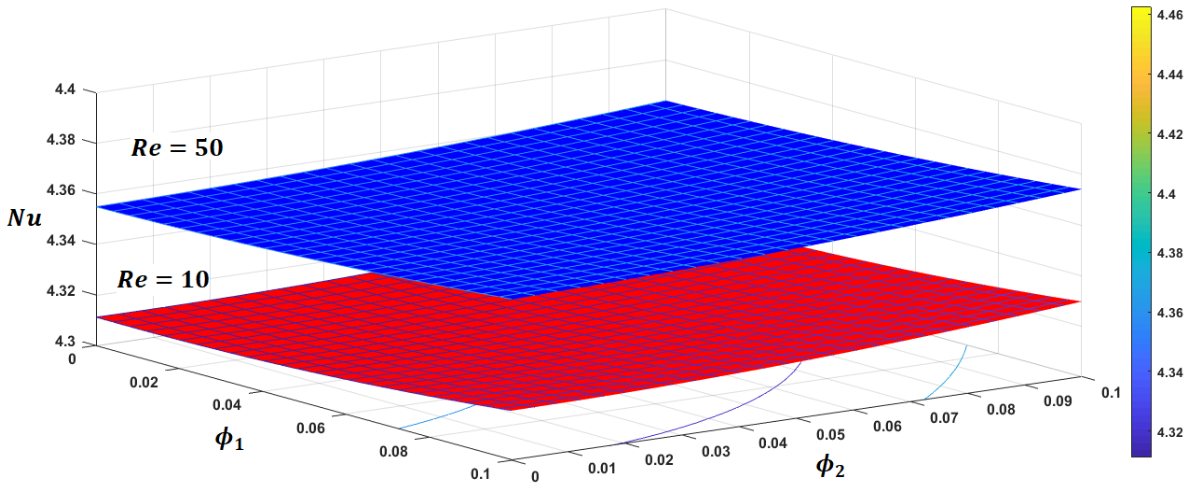

(b)

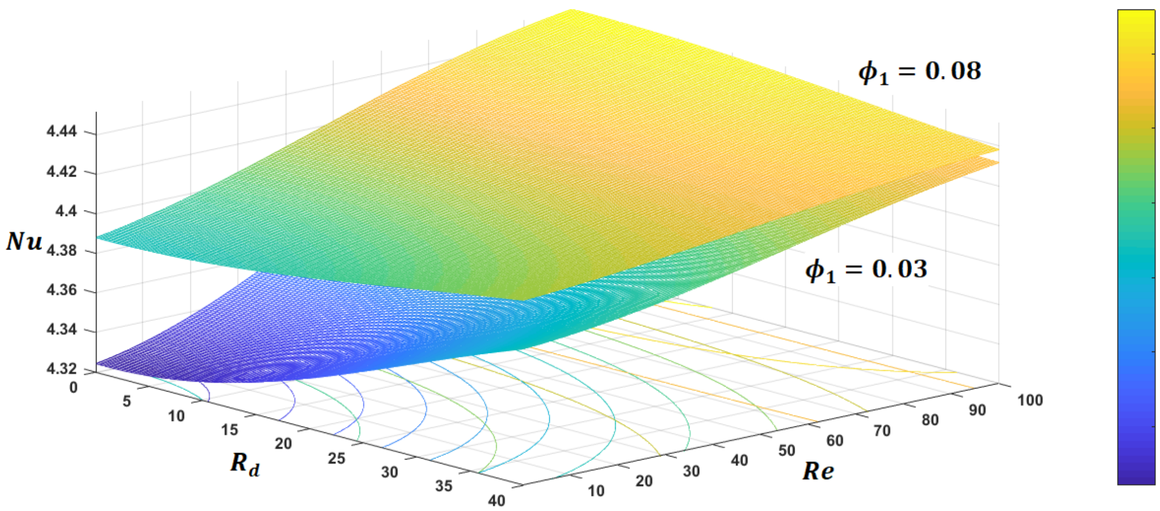

Fig. 8. Variation of average Nusselt number with different pertinent variables.

(a)

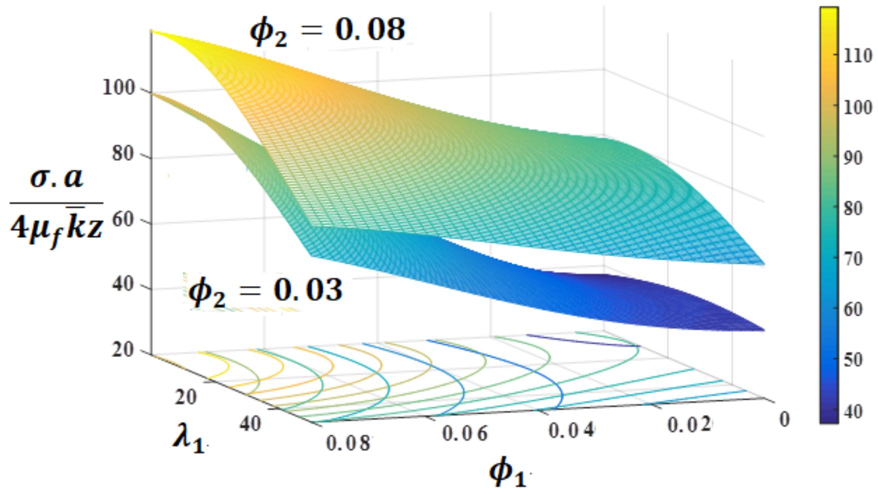

(b)

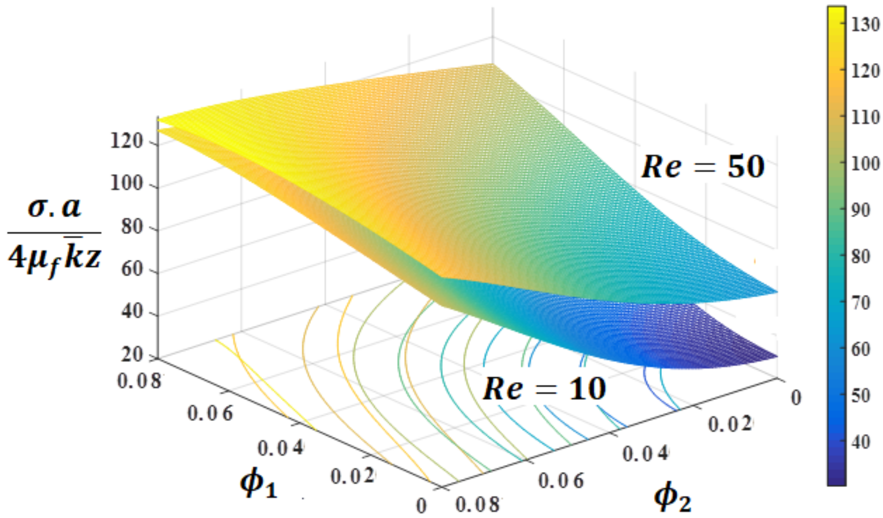

Fig. 9. Variation of dimensionless shear-stress with volumetric concentration of nanoparticles, Reynold number and mixed convection parameter.

(a)

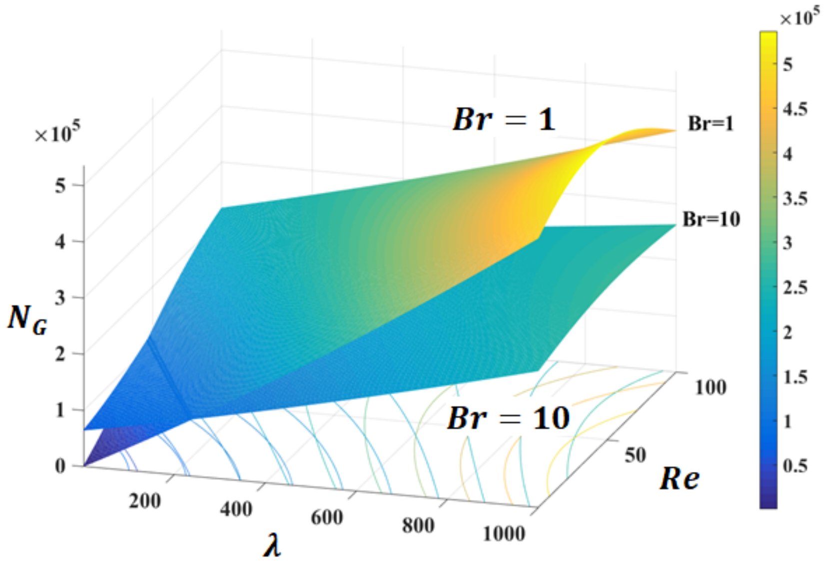

(b)

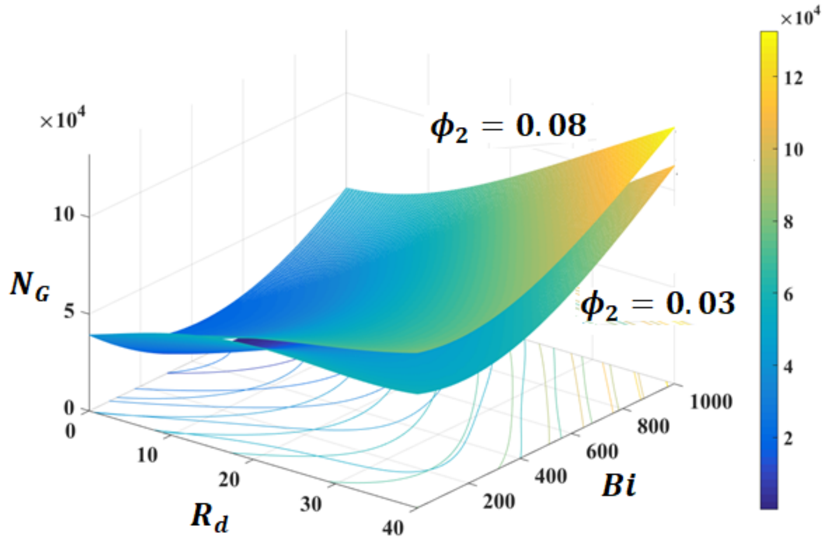

Fig. 10. Variation of entropy generation number with volumetric concentration of nanoparticles, Biot number, Brinkman number, radiation parameter and Reynold number.

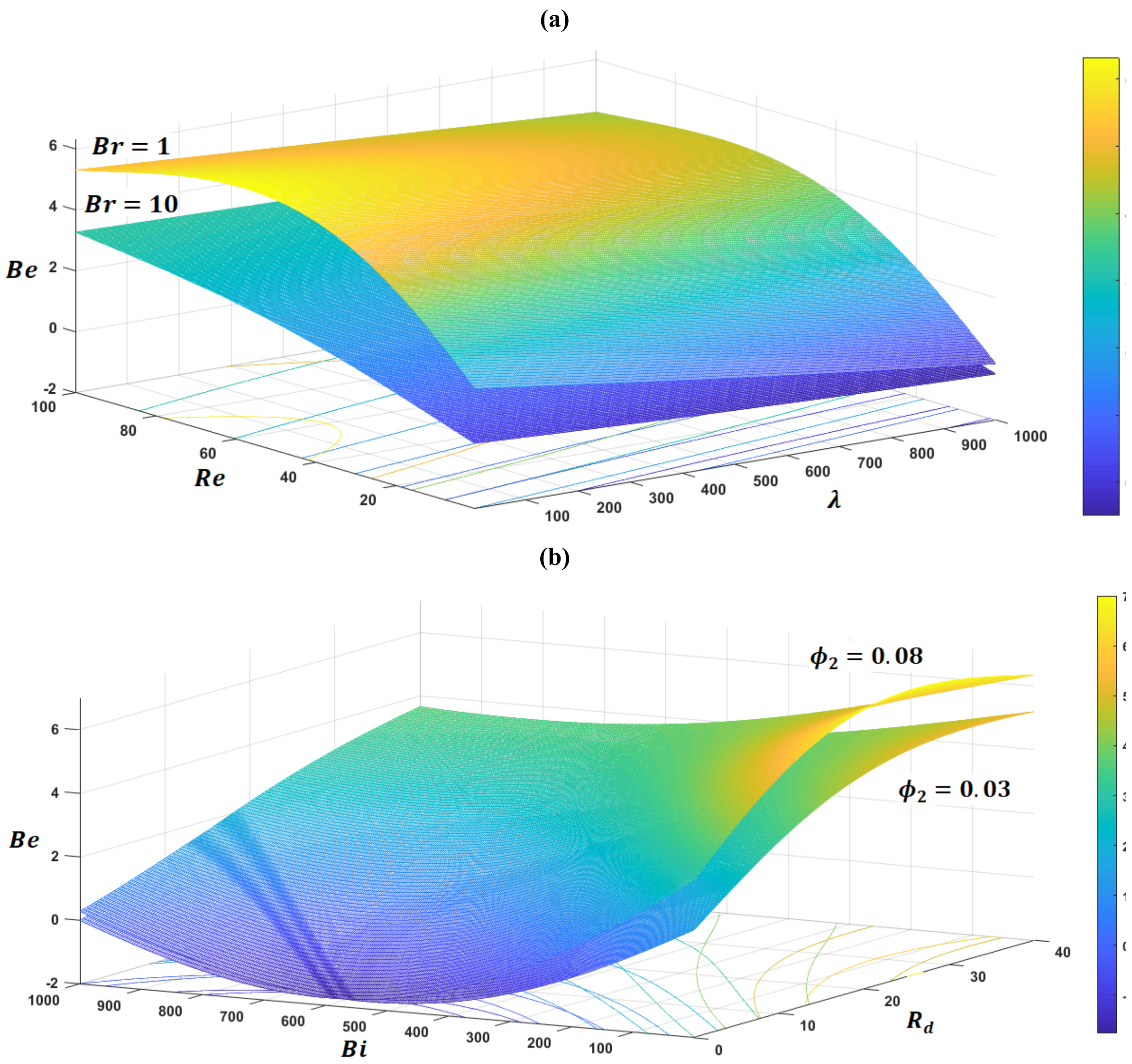

Fig. 11. Variation of Bejan number with the volumetric concentration of nanoparticles, Biot number, radiation parameter, permeability parameter and Reynolds number.

Table 1. Thermo-physical properties of nanofluid and hybrid nanofluid [61]

Properties	Nanofluid	Hybrid Nanofluid
Density	$\rho_{nf} = \rho_f\left[(1-\phi)+\phi\left(\frac{\rho_s}{\rho_f}\right)\right]$	$\rho_{hnf} = \rho_f(1-\phi_2)\left[(1-\phi_1)+\phi_1\left(\frac{\rho_{s_1}}{\rho_f}\right)\right]+\phi_2\rho_{s_2}$
Heat capacity	$(\rho.C_p)_{nf} = (\rho.C_p)_f\left[(1-\phi) + \phi\frac{(\rho.C_p)_s}{(\rho.C_p)_f}\right]$	$(\rho.C_p)_{hnf} = (\rho.C_p)_f(1-\phi_2)\left[(1-\phi_1) + \phi_1\frac{(\rho.C_p)_{s_1}}{(\rho.C_p)_f}\right]+\phi_2(\rho.C_p)_{s_2}$
Viscosity	$\mu_{nf} = \frac{\mu_f}{(1-\phi)^{2.5}}$	$\mu_{hnf} = \frac{\mu_f}{(1-\phi_1)^{2.5}(1-\phi_2)^{2.5}}$
Thermal conductivity	$\frac{k_{nf}}{k_f} = \frac{k_s+(m-1)k_f-(m-1)\phi(k_f-}{k_s+(m-1)k_f+\phi(k_f-k_s)}$	$\frac{k_{hnf}}{k_{bf}} = \frac{k_{s_2}+(m-1)k_{bf}-(m-1)\phi_2(k_{bf}-k_{s_2})}{k_{s_2}+(m-1)k_{bf}+\phi_2(k_{bf}-k_{s_2})}$ $\frac{k_{bf}}{k_f} = \frac{k_{s_1}+(m-1)k_f-(m-1)\phi_1(k_f-k_{s_1})}{k_{s_1}+(m-1)k_f+\phi_1(k_f-k_{s_1})}$

Table 2. Experimental values of density, specific heat and thermal conductivity for base fluid and nanoparticles [62]

Property	Water (*f*)	Al_2O_3	Cu
$\rho\ (\frac{kg}{m^3})$	997.0	3970	8933
$C_p\ (\frac{J}{kg.K})$	4180	765	385
$k\ (\frac{W}{m.K})$	0.6071	40	400

Table 3. The values of sphericity and shape factor of different shapes of nanoparticles [61]

Geometrical appearance		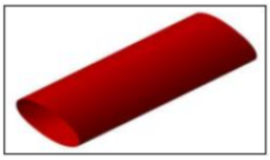	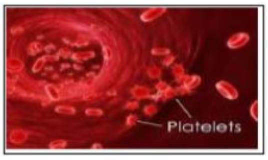
Shape of nanoparticles	Bricks	Cylinders	Platelets
Shape factor (m)	3.7	4.9	5.7
Sphericity	0.81	0.62	0.52

Table 4. The default numerical values of the parameters used in the analysis.

Simulation parameters	η	λ	ε	Re	ϕ_1	Bi	Br	θ_w	γ	ϕ_2	M	R_d	λ_1
	1.45	10	0.9	5.0	0.02	0.1	2.0	1.2	1.5	0.02	3.0	1.0	1.0

Table 5. The order of feature prioritisation applied to Nu

Order of features	1	2	3	4	5	6	7	8	9	10	11	12
Number of feature	Re	Pr	ϕ_1	ϕ_2	Bi	M	R_d	θ_w	λ_1	λ	γ	Br

Table 6. The order of feature prioritisation applied to shear-stress

Order	1	2	3	4	5	6	7	8	9	10	11	12
Number of feature	ϕ_1	ϕ_2	Re	λ	R_d	θ_w	Pr	λ_1	M	Bi	γ	Br

Table 7. The variation range for the parameters included in the Nu correlations.

effective parameters	Re	Pr	ϕ_1, ϕ_2	Bi	M	R_d
	$0.1 \le Re \le 100$	$0.1 \le Pr \le 7$	$0 \le \phi_1, \phi_2 \le 0.08$	$0.1 \le Bi \le 1000$	$3 \le M \le 5.7$	$0 \le R_d \le 40$

Table 8. Nu correlations

Nusselt number correlation	effective parameters	Mean absolute error
$Nu = 1.648 + 0.294 \times Re^{0.975}$	Re	0.7561
$Nu = 1.648 + 0.294 \times Re^{0.975} \times Pr^{0.972}$	Re, Pr	0.3046
$Nu = 1.654 + 0.625 \times Re^{0.976} \times Pr^{0.973} \times {\phi_1}^{0.330}$	Re, Pr, ϕ_1	0.2857
$Nu = 1.678 + 1.451 \times Re^{0.980} \times Pr^{0.977} \times {\phi_1}^{0.332} \times {\phi_2}^{0.371}$	Re, Pr, ϕ_1, ϕ_2	0.2572
$Nu = 1.654 + 1.275 \times Re^{0.976} \times Pr^{0.973} \times {\phi_1}^{0.330} \times {\phi_2}^{0.368} \times Bi^{0.058}$	$Re, Pr, \phi_1, \phi_2, Bi$	0.2224
$Nu = 1.655 + 0.910 \times Re^{0.976} \times Pr^{0.973} \times {\phi_1}^{0.330} \times {\phi_2}^{0.449} \times Bi^{0.058} \times M^{0.400}$	$Re, Pr, \phi_1, \phi_2, Bi$, M	0.2078

Table 9. The variation range for the parameters included in the Nu correlations.

effective parameters	Re	λ	ϕ_1, ϕ_2	R_d	θ_w	Pr
	$0.1 \le Re \le 100$	$1 \le \lambda \le 5000$	$0 \le \phi_1, \phi_2 \le 0.08$	$0 \le R_d \le 40$	$0.6 \le \theta_w \le 3$	$0.1 \le Pr \le 7$

Table 10. Shear-stress correlations

Non-dimensional shear-stress correlations	effective parameters	Mean absolute error
$\frac{\sigma.a}{4\mu_f\bar{k}z} = 35.938 + 258 \times {\phi_1}^{1.478}$	ϕ_1	5.2640
$\frac{\sigma.a}{4\mu_f\bar{k}z} = 28.137 + 1873.14 \times {\phi_1}^{0.9667} \times {\phi_2}^{1.0913}$	ϕ_1, ϕ_2	3.7247
$\frac{\sigma.a}{4\mu_f\bar{k}z} = 32.450 + 1165.62 \times {\phi_1}^{1.200} \times {\phi_2}^{1.375} \times Re^{0.591}$	ϕ_1, ϕ_2, Re	2.3099
$\frac{\sigma.a}{4\mu_f\bar{k}z} = 39.502 + 1791.55 \times {\phi_1}^{1.825} \times {\phi_2}^{1.946} \times Re^{0.9} \times \lambda^{0.318}$	$\phi_1, \phi_2, Re, \lambda$	1.5081
$\frac{\sigma.a}{4\mu_f\bar{k}z} = 35.835 + 1115.47 \times {\phi_1}^{1.470} \times {\phi_2}^{1.585} \times Re^{0.7} \times \lambda^{0.245} \times {R_d}^{3.286}$	$\phi_1, \phi_2, Re, \lambda, R_d$	1.4822
$\frac{\sigma.a}{4\mu_f\bar{k}z} = 35.439 + 1076.15 \times {\phi_1}^{1.442} \times {\phi_2}^{1.557} \times Re^{0.685} \times \lambda^{0.240} \times {R_d}^{1.581} \times {\theta_w}^{0.009}$	$\phi_1, \phi_2, Re, \lambda, R_d, \theta_w$	1.4817

$\frac{\sigma . a}{4\mu_f \bar{k} z} = 35.839 + 1076.15 \times {\phi_1}^{1.442} \times {\phi_2}^{1.557} \times Re^{0.685} \times \lambda^{0.240} \times {R_d}^{1.458} \times {\theta_w}^{0.009} \times Pr^{0.000}$	$\phi_1, \phi_2, Re, \lambda, R_d, \theta_w, Pr$	1.4931

1